

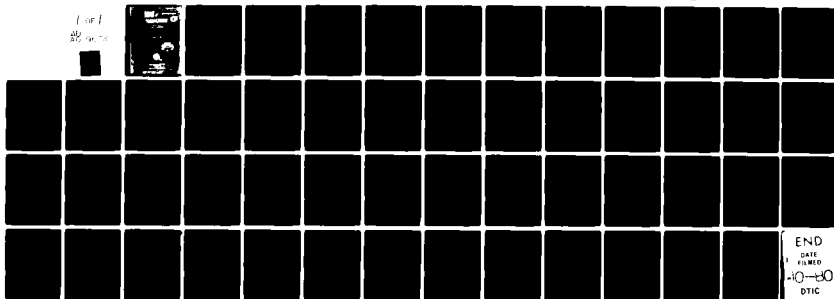
AD-A089 672

NAVAL RESEARCH LAB WASHINGTON DC  
BEAM GENERATED VORTICITY AND CONVECTIVE CHANNEL MIXING.(U)  
SEP 80 J P BORIS, J M PICONE  
UNCLASSIFIED NRL-MR-4327

F/G 20/9

NL

For  
the



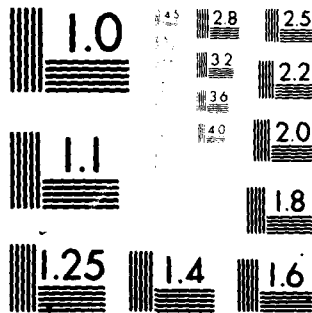
END

DATE

FILED

10-10

DTIC



MICROCOPY RESOLUTION TEST CHART  
NATIONAL BUREAU OF STANDARDS-1963-A

AD A089672

9 Memorandum Rept.

SECURITY CLASSIFICATION OF THIS PAGE (When Data Entered)

14 REPORT DOCUMENTATION PAGE		READ INSTRUCTIONS BEFORE COMPLETING FORM	
1. REPORT NUMBER NRL-MR-4327	2. GOVT ACCESSION NO. AD-A089	3. RECIPIENT'S CATALOG NUMBER 672	
4. TITLE (and Subtitle) BEAM GENERATED VORTICITY AND CONVECTIVE CHANNEL MIXING		5. TYPE OF REPORT & PERIOD COVERED Interim report on a continuing NRL problem	
7. AUTHOR(s) J. P. Boris and J. M. Picone		6. PERFORMING ORG. REPORT NUMBER	
9. PERFORMING ORGANIZATION NAME AND ADDRESS Laboratory for Computational Physics Naval Research Laboratory Washington, DC 20375		8. CONTRACT OR GRANT NUMBER(s)	
11. CONTROLLING OFFICE NAME AND ADDRESS Naval Surface Weapons Center, White Oak Silver Spring, Maryland 20910		10. PROGRAM ELEMENT, PROJECT, TASK AREA & WORK UNIT NUMBERS 62-0580-0-0	
14. MONITORING AGENCY NAME & ADDRESS (if different from Controlling Office) (1253)		12. REPORT DATE September, 1980	
		13. NUMBER OF PAGES 52	
		15. SECURITY CLASS. (of this report) Unclassified	
		15a. DECLASSIFICATION/DOWNGRADING SCHEDULE	
16. DISTRIBUTION STATEMENT (of this Report) Approved for public release; distribution unlimited.			
17. DISTRIBUTION STATEMENT (of the abstract entered in Block 20, if different from Report)			
18. SUPPLEMENTARY NOTES This research was sponsored by the Naval Surface Weapons Center under subtask -80-WRW0190			
19. KEY WORDS (Continue on reverse side if necessary and identify by block number) Charged particle beam Hydrodynamics Gas channel formation Hole boring			
20. ABSTRACT (Continue on reverse side if necessary and identify by block number) Asymmetries in density and pressure gradients exist when a beam deposits energy off center in a hot gaseous channel formed by a previous beam or discharge. These asymmetries, coupled with the natural dynamics of the expanding compound channel, cause vortex filaments to be generated which propagate unabated long after motion would have ceased in a symmetric flow. This concentrated vorticity is a source of convective (turbulent) cooling of the hot channels. In this paper we present a theory for the amount of vorticity generated as a function of asymmetry and system parameters (Continued)			

DD FORM 1 JAN 73 1473

EDITION OF 1 NOV 65 IS OBSOLETE  
S/N 0102-014-6601

SECURITY CLASSIFICATION OF THIS PAGE (When Data Entered)

201720

VB

~~SECRET~~  
SECURITY CLASSIFICATION OF THIS PAGE(When Data Entered)

20. ~~SECRET~~ ABSTRACT (Continued)

and calibrate this theory using detailed numerical simulations. An estimate of the convective mixing time for such composite channels is constructed using the strength of the asymmetry-generated vortex filaments as a source term.

SECURITY CLASSIFICATION OF THIS PAGE(When Data Entered)

## CONTENTS

I.	INTRODUCTION .....	1
II.	MIXING-TIME ESTIMATE .....	4
III.	AN APPROXIMATE VORTICITY INTEGRAL .....	6
IV.	DETAILED NUMERICAL SIMULATIONS .....	15
V.	SUMMARY AND CONCLUSIONS .....	20
	ACKNOWLEDGMENT .....	26
	REFERENCES .....	26

<b>Accession For</b>	
NTIS GRA&I	<input checked="" type="checkbox"/>
DDC TAB	<input type="checkbox"/>
Unannounced	<input type="checkbox"/>
Justification _____	
By _____	
Distribution/ _____	
<b>Availability Codes</b>	
Dist.	Avail and/or special
A	

## BEAM GENERATED VORTICITY AND CONVECTIVE CHANNEL MIXING

### I. INTRODUCTION

Recent theory and numerical computation at NRL have resulted in a theoretical formalism for estimating persistent flows which mix cold ambient air into a beam-heated channel. In this paper we also give a quantitative calibration of that formalism using detailed two-dimensional simulations. The importance of determining the mechanisms and scaling laws governing the dynamics of a gaseous channel heated by a sequence of pulses is clear. One important application is the fixation of atmospheric nitrogen by lightning.

The probable existence of such a cooling mechanism is well documented in NRL laser and discharge data showing heated channels breaking up in a number of circumstances.<sup>1</sup> Data also exists on "turbulent" cooling of multipulse channels from Astron<sup>2</sup> (Fig. 1). The "classical theory" curve in that figure shows that the thermal conduction cooling rate is significantly slower than observed in experiments—pointing to a convective "turbulent" mechanism. Any reasonable estimate of background gas velocities falls orders of magnitude short of explaining the cooling rate, so a mechanism is needed to convert curl-free fluid expansion which cannot mix into persistent vorticity which can.

The symmetric expansion of a cylindrical beam-heated channel causes no convective mixing per se, but asymmetries, appearing either in the beam deposition or as density variations in the background gas, permit the generation of vortex filaments. The sheared flow attending the motion and interaction of these filaments mixes cold background gas into the heated channel at a rate which depends on the strength of the induced vorticity and thus ultimately on the fluid-dynamic asymmetries. Three types of asymmetries can be identified:

1. 2D distortions of the channel from a circular cross section,
2. 2D asymmetries from pulse displacement off the channel axis, and
3. 3D distortions such as characterize a lightning or spark channel.

In this paper we analyze the convective flow and calculate the related mixing rate for the second possibility, a lateral displacement of the second and subsequent pulses from the center of the hot channel created by the first pulse. We then simulate the process numerically to calibrate our analytic results. Figure 2 provides a schematic diagram of the situation which we are considering. A hot circular channel of characteristic radius  $S_0$  and depth  $\rho_\infty/\rho_0$  is assumed to have reached a hydrostatic equilibrium by the time a second pulse comes along displaced to the left by a distance  $X_0$ . The initial characteristic radius of the second pulse channel is  $R_0$  and it expands to  $R_1$ , eventually coming to rest there as a weak acoustic signal continues to propagate off to infinity. This simple 2D situation, shown in cross section in Fig. 2, arises when the second pulse is being driven or is drifting out of the preformed hot, low density channel. Perfectly passive effects such as transverse flows also can cause this displacement.

The radial expansion of the second pulse channel generates vorticity according to the two-dimensional vorticity equation,

$$\frac{\partial \xi_z}{\partial t} + \underline{\nabla} \cdot (\underline{v} \xi_z) = \left[ \frac{\underline{\nabla} \rho \times \underline{\nabla} P}{\rho^2} \right]_z, \quad (1)$$

since the pressure gradient is not aligned with the density gradients present after the first pulse. As depicted in Fig. 3, the resulting velocity distribution will be approximately the same as that of an extended vortex filament pair located at  $(\bar{x}, \pm \bar{y})$  and having respective strengths  $\pm \bar{V}$ , where

$$\bar{V}(t) = \int_0^\infty dy \int_{-\infty}^\infty dx \xi_z(x, y, t). \quad (2)$$

The bar over capital,  $\bar{V}$ , has units of  $\text{cm}^2/\text{sec}$  and is an area integrated vorticity, to be distinguished from lower case  $v$  and  $\underline{v}$ , which are velocities and have units of  $\text{cm}/\text{sec}$ . Because of the two-dimensional Cartesian geometry, only the  $z$  component of vorticity,  $\xi_z$ , need be considered.



The vortex pair shown in Fig. 3 propagates horizontally at a speed which is roughly 1/4 that of the fluid jetting along the  $x$  axis between the two oppositely rotating filaments. The time it takes a fluid element at one side of the original channel (say  $x = S_0$ ) to reach the other side ( $x = -S_0$ ) will be used as a measure of the mixing time  $\tau_{\text{mix}}$ . The resulting mixing time formula coupled with our analytic approximation for the strength of the vortex filaments formed, gives a simple yet quite accurate expression for scaling laws and quantitative estimates.

In the next section the mixing time formula will be derived by analyzing the system shown in Fig. 3. This formula is then coupled with a dimensional-analysis approximation of the expansion-induced vorticity to show that mixing of cool background gas with the heated channel interior due to this vorticity occurs on short timescales, relative to the cooling from molecular thermal conduction. The third section analyzes the configuration of Fig. 2 and arrives at a useful analytic expression for the induced vorticity to replace the less accurate dimensional analysis for  $\bar{V}(\tau)$  used to obtain the preliminary estimates in Section II. This analysis gives variations of integrated vorticity  $\bar{V}$  with the non-dimensional parameters characterizing the pulse strength, the lateral pulse displacement, the relative channel sizes, and the original heated channel depth, all of which cannot be deduced from dimensional considerations alone.

Section IV presents the results of detailed two-dimensional simulations of the problem depicted schematically in Fig. 2. These computations not only validate the qualitative features predicted by the analytic model, but they also allow us to calibrate the total vorticity integral quantitatively for strong pulses. This allows us to define a meaningful channel expansion velocity needed for the theory. Applications of these calibrated formulae to NRL and LLL data in Section V indicate as good agreement between predicted mixing times and observed mixing times (typically within a factor of two) as can reasonably be expected.

## II. MIXING-TIME ESTIMATE

We assume that the asymmetry induced flow field may be represented approximately as two compact vortex filaments of strength  $\pm \bar{V}$  at  $\pm \bar{y}$ . The azimuthal velocity induced by each of these decays as  $1/r$  away from the vortex center. The velocity of the fluid along the symmetry plane is the sum of flows induced by each vortex separately. Figure 3 is a schematic of the situation with a sketch of the variation of the fluid flow velocity along the  $x$ -axis shown. This velocity is given by

$$v_x(x, 0) = 2v_\theta \cos\theta = \frac{\bar{V}}{\pi} \frac{\cos\theta}{\sqrt{x^2 + \bar{y}^2}} = \frac{\bar{V}}{\pi} \frac{\bar{y}}{x^2 + \bar{y}^2} \quad (3)$$

where  $\cos\theta \equiv \bar{y}/\sqrt{x^2 + \bar{y}^2}$ . The filaments are migrating in the same direction at a slower velocity,

$$v_x(0, \bar{y}) = \frac{\bar{V}}{4\pi\bar{y}} \quad (4)$$

which we will ignore in the following integral estimates. This overall migration velocity will become important when a series of pulses is being considered. In that case a quasi-steady state develops in which the systematic migration of the integrated vorticity entrains cold fluid stochastically at the edges of the hot turbulent channel.

To estimate the mixing time, we use Eq. (3) to calculate the time it takes a fluid element starting at  $x = -S_0$  to reach  $x = S_0$ . The equation of motion for this element is

$$\frac{dx}{dt} = v_x(x, 0) = \frac{\bar{V}}{\pi} \frac{\bar{y}}{(x^2 + \bar{y}^2)} \quad (5)$$

which can be integrated to give

$$\int_0^\tau dt \equiv \tau_{\text{mix}} = \frac{\pi}{\bar{V}\bar{y}} \int_{-S_0}^{S_0} dx (x^2 + \bar{y}^2). \quad (6)$$

The quadrature can be performed and gives the following mixing time estimate:

$$\tau_{\text{mix}} = \frac{2\pi}{|\bar{V}|} \frac{S_0}{\bar{y}} \left[ \frac{S_0^2}{3} + \bar{y}^2 \right], \quad (7)$$

where the vortex strength  $\bar{V}$  is given by Eq. (2) and the "average" displacement of this vorticity above the  $y = 0$  plane is given formally by

$$\bar{y} \equiv \frac{1}{\bar{V}} \int_0^\infty dy \int_{-\infty}^\infty dx y \xi_z(x, y). \quad (8)$$

To complete this estimate we need expressions for  $\bar{V}$  and  $\bar{y}$  generated by the off-center expansion of the second pulse channel. The remainder of this paper is concerned with calculating analytically and calibrating numerically an expression for  $\bar{V}$ . A simple dimensional analysis allows us to make at least crude estimates rather directly. From Eq. (1) it would appear that a number of size scales enter the problem:  $S_0$ , the radius of the channel created by the first pulse; the characteristic scale lengths for the pressure and density gradients; and the initial and final radii  $R_0$  and  $R_1$  of the second, displaced channel being formed. Fortunately most of these scales are either unimportant or expressible in terms of  $S_0$ . If the first and second pulse deposit a like amount of energy,  $R_1$  and  $S_0$  will be roughly equal and  $R_0$  will be a modest fraction of  $R_1$ . In the numerical simulations (Fig. 7), the second pulse initial radius  $R_0 = 0.4$  cm,  $S_0 = 1.0$  cm, and the overpressure factor for the first pulse was 30. In this situation pressure balance is achieved (adiabatically) when the density drops by a factor of 11.6 and the radius  $R_0$  increases to  $R_1 \sim 1.4$  cm  $\sim S_0$ .

Other simplifications are expected. Whether a shock expansion or an adiabatic expansion is being driven by the energy deposition, the larger the pressure gradient the smaller the time over which it acts. Thus the integrated vorticity is relatively insensitive to the shock thickness. Similarly, the density gradient is integrated over space so the inner and outer densities enter,  $\rho_0$  and  $\rho_\infty$ , but the scale length of the transition region (shown in Fig. 6 as a band centered at  $S = S_0$ ) can be neglected. It is reasonable to expect and will in fact be shown that the maximum vorticity generation occurs when  $X_0 \sim S_0$ . Thus there are no small parameters arising as ratios of characteristic lengths unless we consider exceptionally tightly focussed pulses in which case  $R_0 \ll R_1 \sim S_0$  or only slight departures from the symmetric superposition of the pulses in which case  $X_0 \ll S_0$ .

The integrated vorticity  $\bar{V}$  has units of  $\text{cm}^2/\text{sec}$ , a length times a velocity or a characteristic time multiplied by a velocity squared. The characteristic velocity will be the expansion velocity. When the energy deposition is fast, as in the problem of interest here, this velocity is a characteristic sound speed  $c_s$ . The characteristic time is the expansion duration (if the energy deposition is slow) or the sonic transit time  $S_0/c_s$ . Thus we expect

$$\bar{V} = c_s S_0 F \quad (9)$$

where  $F$  is a dimensionless form factor containing geometric effects, detailed hydrodynamics interactions, and information about the channel and beam profiles. Cancellation effects leaving  $\underline{v} \cdot \underline{\nabla} \underline{v}$  as the dominant contribution to the vorticity source term generally reduce  $F$  somewhat below unity. This will be demonstrated below.

If we assume that  $\bar{y} \approx \sqrt{\frac{2}{3}} S_0$ , Eq. (7) for the mixing time becomes

$$\tau_{\text{mix}} \approx \sqrt{6} \pi \frac{S_0}{c_s F} \sim 7.7 \frac{S_0}{c_s F} \quad (10)$$

For a strong pulse which heats the gas appreciably on passage, we shall assume  $F \sim \frac{1}{2}$ . Taking  $5 \times 10^4$  cm/sec as a generic value for  $c_s$  and choosing  $S_0 = 1$  cm gives

$$\tau_{\text{mix}} \sim \frac{7.7 \times 1}{5 \times 10^4 \times \frac{1}{2}} \approx 300 \mu\text{sec}.$$

This 300  $\mu\text{sec}$  "mixing time" from the dimensional analysis estimate of Eq. (10) is the time for cold material from one side of a hot channel to cross the channel and reach the other side. True mixing of hot and cold fluid will probably take somewhat longer because one or two rotations of the vortices will be required to entrain and smear in an appreciable amount of the colder fluid. This "mixing" time, however it is best defined, is clearly important when comparable to only a few pulse separation times.

In the next section an integration of the vorticity source term in Eq. (1) is performed to improve on Eqs. (9) and (10), our dimensional analysis estimates. Using a few reasonable assumptions, a quadrature for integrated vorticity  $\bar{V}$  is obtained which will display the various non-dimensional dependences of the form/fudge factor  $F$  in Eqs. (9) and (10).

### III. AN APPROXIMATE VORTICITY INTEGRAL

Equation (2) defines the integrated vortex strength at any instant in time and will be used in conjunction with Eq. (1) to develop an approximate analytic expression to replace Eq. (9) in the mixing

time estimate Eq. (7). For our purposes we only need  $\bar{V}(\tau)$ , where  $\tau$  is a time sufficiently long that expansion and vorticity generation is complete. Using the geometry of Fig. 1,

$$\bar{V}(\tau) = \int_0^\tau dt \int_0^\pi d\theta \int_{R(t)}^\infty r dr \left[ \frac{\nabla \rho \times \nabla P}{\rho^2} - \xi \nabla \cdot \underline{V} \right]_z \quad (11)$$

where the spatial integral is performed over the fluid outside the expanding cylinder  $R_0 \leq R(t) \leq R_1$ .

We assume that this outside region ( $r > R(t)$ ) behaves incompressibly and the inside, beam-heated region expands uniformly. Thus

$$\begin{aligned} v_r(r,t) &= \frac{U(t)r}{R(t)} \text{ for } r \leq R(t) & \text{and} \\ v_r(r,t) &= \frac{U(t)R(t)}{r} \text{ for } r \geq R(t) \end{aligned} \quad (12)$$

specifies the flow everywhere as a function of the heated region radius  $R(t)$  and velocity  $U(t) \equiv \dot{R}(t)$ . This flow has a uniform but time-varying divergence inside the heated region and zero divergence outside. In fact, the fluid inside the just-heated channel will give up energy to the cold surrounding fluid via shocks and a fraction of the pulse-deposited energy will even escape to  $\infty$  as an acoustic wave. The smooth shape of the expanded channels observed from 1D hole-boring calculations<sup>3</sup> and the computational fact that most of the deposited energy stays close to the original pulse deposition lends hope for the approximations implied by using the flow field (12).

As will soon be shown somewhat more explicitly, the important feature of vorticity generation is how far radially each fluid element moves. Pressure gradients arising from accelerations of a fluid element do not really contribute to vorticity in the present context. Because the fluid elements begin and end their expansion-induced displacement at rest, the average acceleration is zero. The  $\underline{v} \cdot \nabla \underline{v}$  vorticity source term has the same sign throughout the expansion and consequently contributes more strongly to the integrated vorticity.

The velocity field (12) can be substituted into the fluid momentum equation for the outside region and yields

$$\begin{aligned} \frac{dv_r}{dt} &= \frac{\partial v_r}{\partial t} + v_r \frac{\partial v_r}{\partial r} = \frac{1}{r} \frac{\partial(UR)}{\partial t} - \frac{U^2 R^2}{r^3} \\ &= -\frac{1}{\rho} \nabla_r P. \end{aligned} \quad (13)$$

Since we are going to assume the motion behaves incompressibly in the outer region  $r > R(t)$ , the second term on the right hand side of Eq. (11) vanishes simplifying the integral considerably. The acceleration is being taken in the radial direction with values strictly appropriate only when feedback of the asymmetric density gradients on the driving expansion flow are small.

The theoretical model appears to work quite well for large density variations as well, a result that is understandable in hindsight. The maximum vortex-induced flow speed which resides in the system is much smaller than the maximum expansion speed. The vorticity is generated essentially instantaneously relative to the mixing timescale  $\tau_{\text{mix}}$ . Thus the generation term can be calculated assuming that the initial asymmetric density gradients do not change the expansion-driven pressure gradients and that the vorticity which develops does not affect the density gradients during the relatively brief expansion.

Under these assumptions only the density gradient in the  $\theta$  direction need be crossed with the radial pressure gradients. Using Eq. (13) and

$$\nabla_{\theta} \rho = \frac{1}{r} \frac{\partial \rho}{\partial \theta} \quad (14)$$

in Eq. (11) we obtain

$$\bar{V}(\tau) = \int_0^\tau dt \int_0^\pi d\theta \int_{R(t)}^\infty dr r \left[ -\frac{1}{\rho r} \frac{\partial \rho}{\partial \theta} \right] \left[ \frac{(UR)^2}{r^3} - \frac{1}{r} \frac{\partial(UR)}{\partial t} \right]. \quad (15)$$

We now change to the Lagrangian variables  $(r_0, \theta_0)$  where

$$\begin{aligned} r - r(t) &= \sqrt{r_0^2 + R^2(t) - R_0^2} \quad \text{and} \\ \theta &= \theta_0. \end{aligned} \quad (16)$$

Then

$$r dr = r_0 dr_0 \quad (17)$$

and  $r(t)$  is the instantaneous radial position of a fluid element initially at  $r(0) = r_0$ . Because the flow described by Eq. (12) is incompressible, the continuity equation becomes

$$\frac{d\rho}{dt} = -\rho \nabla \cdot V = 0, \quad (18)$$

and therefore

$$\rho(r(t), \theta) = \rho(r_0, \theta). \quad (19)$$

Thus Eq. (15) becomes

$$\bar{V}(\tau) = \int_0^\tau dt \int_0^\pi d\theta \int_{R_0}^\infty dr_0 r_0 \left[ -\frac{1}{\rho r(t)} \frac{\partial \rho}{\partial \theta}(r_0, \theta) \right] \left[ \frac{(UR)^2}{r^3(t)} - \frac{1}{r(t)} \frac{\partial (UR)}{\partial t} \right]. \quad (20)$$

Note that the  $\theta$  gradient of  $\rho$  decreases as the expansion proceeds because the fluid elements are moving to larger radius while retaining the same  $\theta$  variation.

At this point we assume a general form for the density profile  $\rho(s)$  in the original low density channel.

$$\rho(s) = \rho_\infty e^{-\ln\left(\frac{\rho_\infty}{\rho_0}\right) g(s/s_0)} \quad (21)$$

where

$$s = X_0^2 + r_0^2 - 2X_0 r_0 \cos \theta, \quad (22)$$

$$g(0) = 1 \text{ and } g(\infty) = 0.$$

Then

$$\frac{\nabla_\theta \rho}{\rho} = \frac{1}{r\rho} \frac{\partial \rho}{\partial \theta} = -\ln\left(\frac{\rho_\infty}{\rho_0}\right) \frac{1}{r} \frac{\partial g(s)}{\partial \theta} \quad (23)$$

and the  $\theta$  integral in Eq. (15) can be performed without approximation.

This gives us

$$\begin{aligned} \int_0^\pi d\theta \frac{\partial g}{\partial \theta} &= g(s(r_0, \pi)) - g(s(r_0, 0)) \\ &= \begin{cases} g(r_0 + X_0) - g(X_0 - r_0) & r_0 \leq X_0 \\ g(r_0 + X_0) - g(r_0 - X_0) & r_0 > X_0 \end{cases} \end{aligned} \quad (24)$$

and Eq. (20) becomes

$$\begin{aligned} \bar{V}(\tau) = \ln \left( \frac{\rho_\infty}{\rho_0} \right) \int_0^\tau dt \left\{ \int_{R_0}^\infty \frac{dr_0 r_0}{r^2(t)} \left[ \frac{(UR)^2}{r^2(t)} - \frac{\partial(UR)}{\partial t} \right] g(r_0 + X_0) \right. \\ \left. - \int_{R_0}^{X_0} \frac{dr_0 r_0}{r^2(t)} \left[ \frac{(UR)^2}{r^2(t)} - \frac{\partial(UR)}{\partial t} \right] g(X_0 - r_0) - \int_{X_0}^\infty \frac{dr_0 r_0}{r^2(t)} \left[ \frac{(UR)^2}{r^2(t)} - \frac{\partial(UR)}{\partial t} \right] g(r_0 - X_0) \right\} \end{aligned} \quad (25)$$

Still working on this rather general form of the equation, approximations must be made to get a useable analytic result because Eq. (25) is a hairy 2D quadrature even assuming that the appropriate  $R(t)$  for our particular case is known. The approximation most useful is to evaluate the integrand at one time. If we assume  $U(\tau) = U(0) = 0$  so that the initial and final states of the expansion are at rest, the term  $\frac{\partial}{\partial t}(UR)$  integrates to zero. To approximate  $\bar{V}(\tau)$ , let us evaluate  $r(t)$  in the integrand at the time  $t_m$  when the expansion flux  $R_m U_m \equiv R(t_m) U(t_m)$  is maximum. Then the  $\frac{\partial}{\partial t}(UR)$  term vanishes and  $r(t)$  is still a function of  $r_0$ , the initial fluid element radius, but not a function of  $t$ .

$$r_m \equiv \sqrt{r_0^2 + R_m^2 - R_0^2}. \quad (26)$$

The desired integral becomes

$$\begin{aligned} \bar{V}(\tau) = \ln \left( \frac{\rho_\infty}{\rho_0} \right) \int_0^\tau dt U^2(t) R^2(t) \left\{ \int_{R_0}^\infty \frac{dr_0 r_0}{r_m^4} g(r_0 + X_0) \right. \\ \left. - \int_{R_0}^{X_0} \frac{dr_0 r_0}{r_m^4} g(X_0 - r_0) - \int_{X_0}^\infty \frac{dr_0 r_0}{r_m^4} g(r - X_0) \right\}. \end{aligned} \quad (27)$$

In Eq. (27) the time integral can be simply approximated as  $U_m^2 R_m^2 \tau/2$  where  $\tau = 2(R_1 - R_0)/U_m$ .

Thus

$$\begin{aligned} \bar{V}(\tau) = \frac{U_m^2 \tau}{2} \ln \left( \frac{\rho_\infty}{\rho_0} \right) \left\{ \int_{R_0}^\infty dr_0 r_0 \frac{R_m^2 g(r_0 + X_0)}{(r_0^2 + R_m^2 - R_0^2)^2} \right. \\ \left. - \int_{R_0}^{X_0} dr_0 r_0 \frac{R_m^2 g(X_0 - r_0)}{(r_0^2 + R_m^2 - R_0^2)^2} - \int_{X_0}^\infty dr_0 r_0 \frac{R_m^2 g(r_0 - X_0)}{(r_0^2 + R_m^2 - R_0^2)^2} \right\}. \end{aligned} \quad (28)$$



Now the integral is written in terms of three non-dimensional parameters

$$\begin{aligned} a &\equiv R_0/R_m < 1, \\ b &\equiv R_m/S_0 \leq 1, \text{ and} \\ c &\equiv X_0/S_0 \sim 1, \end{aligned} \quad (29)$$

where  $S_0$  is a characteristic scale length for variation of  $g(s/S_0)$  and hence of the original channel density profile, Eq. (21). Letting the integration variable be  $\eta \equiv r/R_m$  yields

$$\begin{aligned} \bar{V}(\tau) = \frac{U_m^2 \tau}{2} \ln \left( \frac{\rho_\infty}{\rho_0} \right) &\left\{ \int_a^\infty d\eta \eta \frac{g(S_0[\eta b + c])}{(1 + \eta^2 - a^2)^2} \right. \\ &\left. - \int_a^{c/b} d\eta \eta \frac{g(S_0[c - \eta b])}{(1 + \eta^2 - a^2)^2} - \int_{c/b}^\infty d\eta \eta \frac{g(S_0[\eta b - c])}{(1 + \eta^2 - a^2)^2} \right\} \end{aligned} \quad (30)$$

If the remaining composite integral is identified as a three parameter form factor  $f_2(a,b,c)$  with values of order unity and if  $U_m = c_s$ , an assignment which will be justified empirically by detailed numerical simulation in the next section for strong pulses, the very useful improvement on the dimensional approximation Eq. (9) is obtained:

$$\bar{V}(\tau) \approx c_s (R_1 - R_0) \ln \left( \frac{\rho_\infty}{\rho_0} \right) f_2(a,b,c). \quad (31)$$

Here the form factor  $f_2$ , defined as

$$\begin{aligned} f_2(a,b,c) &\equiv \int_a^\infty d\eta \eta \frac{g(S_0[\eta b + c])}{(1 + \eta^2 - a^2)^2} - \int_a^{c/b} d\eta \eta \frac{g(S_0[c - \eta b])}{(1 + \eta^2 - a^2)^2} \\ &\quad - \int_{c/b}^\infty d\eta \eta \frac{g(S_0[\eta b - c])}{(1 + \eta^2 - a^2)^2}, \end{aligned} \quad (32)$$

is generally less than 1/2. The sign of  $f_2$  indicates the direction of flow in the  $x,y$ -plane—counterclockwise or clockwise.

The general integral form factor, Eq. (32), can be integrated numerically for any reasonable profile  $g(s/S_0)$ . Figure 4 shows plots of  $f_2$  versus  $c$ , the measure of channel separation for several values of  $a$  at  $b = 0.7$  and for several values of  $b$  at  $a = 0.6$ , values closely approximating the actual initial conditions for the detailed calculation of the next section. In this figure the super Gaussian profile was used,

$$g_{SG}(s/S_0) = e^{-s^2/S_0^2} \quad (33)$$

and the integrations performed using a numerical quadrature algorithm. Calculations have also been carried out using a Bennett profile,

$$g_B(s/S_0) = \frac{-\ln[1 - \frac{\rho_\infty - \rho_0}{\rho_\infty} / (1 + s^2/S_0^2)^2]}{\ln\left(\frac{\rho_\infty}{\rho_0}\right)} \quad (34)$$

and are plotted in Figure 5. In the degenerate case of a square well density discontinuity at  $s = S_0$ ,

$$g_{SW}(s/S_0) = \begin{cases} 0 & \text{if } s \geq S_0 \\ 1 & \text{if } s < S_0. \end{cases} \quad (35)$$

the integral can be performed analytically to give

$$f_{SW}(a,b,c) = \frac{1}{2} \left[ \frac{b^2}{(1+c)^2 + b^2(1-a^2)} - \frac{b^2}{(1-c)^2 + b^2(1-a^2)} \right] \quad (36)$$

for  $ab < c - 1$ . This is the case when the second pulse is wholly outside the channel formed by the first pulse. As  $c$  approaches  $\infty$ ,  $f_D$  decreases as  $-1/c^2$  so pulse channels separated by more than 3 radii interact only weakly.

When the channels are closer,  $ab > c - 1$  and the channels overlap somewhat initially. When  $-ab < c - 1$  there is still part of the second channel of initial radius  $R_0$  outside the cylinder  $s = S_0$  so

$$f_{SW}(a,b,c) = \frac{1}{2} \left[ \frac{b^2}{(1+c)^2 + b^2(1-a^2)} - 1 \right]. \quad (37)$$

Equation (37) agrees with (36) at the interfacial separation  $c = 1 + ab$ .

There is a third region when the initial radius of the second channel lies wholly within the first, i.e.,  $S_0 > X_0 + R_0$  or  $1 > c + ab$ . Then  $f_{SW}(a,b,c)$  satisfies Eq. (36) again. The cross over point at  $c + ab = 1$  again has the two expressions equal. In the intermediate region ( $1 - ab \leq c \leq 1 + ab$ ),  $f_{SW}$  takes on its peak (negative) value at the exterior touching point  $c = 1 + ab$ . For larger values of  $c$  the magnitude  $|f_{SW}|$  decreases and for smaller values  $|f_{SW}|$  decreases monotonically to zero at  $c = 0$ . This peak negative value is

$$f_{SW \max} = \frac{-2(1+ab)}{(4+4ab+b^2)} \quad (38)$$

When  $ab = b^2 = 1/2$ ,  $|f_{SW}|_{\max} = 6/13$  which is close to the values in Figs. 4 and 5 for  $f_{SG}$  and  $f_B$  respectively.

Also of interest is the slope  $\frac{\partial f}{\partial c}$  at  $c = 0$  where the pulses are concentric and no vorticity generation is expected:

$$\left. \frac{\partial f}{\partial c} \right|_{c=0} = \frac{-2b^2}{1+b^2(1-a^2)} \quad (39)$$

which is non-zero and large. Thus even modest non-concentricity leads to appreciable vorticity and mixing. Similar behavior is observed in the two smooth profiles considered as well. Figure 6 compares  $f_B \left( \frac{1}{\sqrt{2}}, \frac{1}{\sqrt{2}}, c \right)$ ,  $f_{SG} \left( \frac{1}{\sqrt{2}}, \frac{1}{\sqrt{2}}, c \right)$  and  $f_{SW} \left( \frac{1}{\sqrt{2}}, \frac{1}{\sqrt{2}}, c \right)$  to demonstrate the similarity among the vorticity generation form factors regardless of the profile. This relative profile insensitivity arises because  $\bar{V}$  is an integral quantity, the total upper half plane circulation.

Returning to our integrated vorticity estimate of Eq. (31) with a maximum form factor of 6/13,

$$|\bar{V}|_{\max} \approx \frac{6}{13} c_s (R_1 - R_0) \ln \left( \frac{\rho_\infty}{\rho_0} \right) \quad (40)$$

Using  $v_{jet}$  as the maximum on axis velocity and assuming  $\bar{y} \approx R_1 - R_0$  gives

$$|v_x|_{\max} \approx \frac{6}{13\pi} \ln \left( \frac{\rho_\infty}{\rho_0} \right) c_s \quad (41)$$

Under optimum conditions the velocity between the vortex filaments approaches a quarter of the sound speed in the surrounding fluid. When the expansion is subsonic throughout (where this analysis ought to be most accurate),  $c_s$  in Eq. (41) should be replaced by the appropriately averaged expansion velocity  $U_m$ .

Using Eq. (7) for the mixing time with  $\bar{y} \approx \sqrt{\frac{2}{3}} S_0 \approx R_1 - R_0$  and  $|\bar{V}|_{\max}$  from Eq. (40) above gives

$$\tau_{\text{mix}}^{\text{min}} \approx \frac{13\pi S_0}{2c_i \ln \left( \frac{\rho_{\infty}}{\rho_0} \right)}. \quad (42)$$

With  $c_i \approx 5 \times 10^4$  cm/sec,  $\ln(\rho_{\infty}/\rho_0) \approx 2.5$ , and  $S_0 = 1$  cm, the fastest mixing time is seen to be about 160  $\mu$ sec. This estimated fastest mixing time is within a factor of two of the dimensional estimate. In any particular system the integral of Eq. (32) can be performed numerically and the resulting form factor substituted into Eq. (25) for the integrated vorticity.

The sign of  $\bar{V}(\tau)$  is negative for the configuration of Fig. 2 where the second pulse is centered to the left of the original channel. This means that the jet of colder wall gas across the original channel starts on the side opposite to the displaced second pulse and rushes toward the newly heated region. On average the old channel moves toward the new channel. This average motion does not imply mixing but the spatial behavior of the flow from the vortex filament pair, as will be seen in the simulations of Section IV, effectively bisects the composite hot channel with a cold jet. The result is two smaller channels above and below the original symmetry plane in which the vortex filaments are now centered. A third pulse located at  $y = 0$  between the two modified channels will cause each of these smaller channels to bifurcate again with fluid jets from the top of the upper channel and the bottom of the lower channel impinging on the third expanding channel from above and below.

In the next section the problem of Fig. 7 is solved numerically with  $\rho_{\infty}/\rho_0 = 10$ ,  $R_0 = 0.4$  cm,  $R_1 = 1.4$  cm,  $S_0 = 1.0$  cm, and  $X_0 = 1.0$  cm. If we assume  $R_{11} \sim 1.0$  cm,  $a \sim 0.4$ ,  $b \sim 1.0$ ,  $c = 1.0$ , then  $f_2(.4, 1.0, 1.0) \approx -1/5$  from Fig. 16. Substituting these numbers into Eq. (31) with  $c_i$  taken as  $5 \times 10^4$  cm/sec gives  $\bar{V}(\tau) \approx -2.3 \times 10^4$  cm<sup>2</sup>/sec. This number is within 10% of the measured value  $-2.1 \times 10^4$  cm<sup>2</sup>/sec (Section IV). The value of  $c_i$  used should be evaluated in the original channel density and temperature profiles at the location of the center of the second pulse, i.e.,  $x = -X_0 = -1$  cm for the example here. The characteristic time  $\tau$  must be equal to  $(R_1 - R_0)/(c_i/2) \sim 25$   $\mu$ sec to justify using  $c_i$  as the effective maximum expansion velocity of the heated cylinder. This value is also within 10% of the observed value of  $\tau \leq 30$   $\mu$ sec.

Using Eq. (3) with  $x = 0$  gives the maximum flow velocity expected in the symmetry plane,

$$v_{x_{\max}} = \frac{\bar{V}(\tau)}{\pi \bar{y}} \approx -90 \text{ m/sec}, \quad (43)$$

when  $\bar{y} = \sqrt{\frac{2}{3}}$  cm. This value is in good agreement with the measured jet velocity of  $-85 \text{ m/sec}$  seen in the detailed simulations. The mixing time calculated from Eq. (7) for these parameters is about  $330 \mu\text{sec}$ .

#### IV. DETAILED NUMERICAL SIMULATIONS

*Preliminary* detailed numerical simulations of this problem have been performed using the FAST2D<sup>4,5,6</sup> computer code to validate and calibrate the approximate analytic model developed above. In addition to accounting for shocks properly, which the theoretical model does not do, the simulations are capable of describing the late-time motions and profiles as modified by the induced vorticity. Thus the various elements of the mixing-time approximations, and their significance, can be evaluated using detailed calculations of representative problems. In this paper we restrict ourselves to a few calculations related to the specific configuration of Fig. 7 to calibrate and validate the most questionable assumptions leading to Eq. (28). Questions of channel cooling and complex multipulse flows are left for future studies.

The calculations based on fig. 7 used Cartesian coordinates on a stationary rectangular grid consisting of 100 by 30 cells of dimensions  $\delta x$  and  $\delta y$ , each varying from 1 mm to 5 mm. As shown in Figs. 8 and 9, an embedded, finely zoned region of  $50 \times 20$  cells 1 mm on a side was centered on the initial 1.0 cm radius hot channel. With increasing distance from the center of the channel, the values of  $\delta x$  and  $\delta y$  transitioned smoothly from 1 mm to 5 mm. Near the sides and top of the grid,  $\delta x$  and  $\delta y$  were both 5 mm.

Figure 10 shows a plot of  $\rho(x, 0, 0)$  and  $P(x, 0, 0)$  along the  $y = 0$  plane at the time the second pulse is deposited. Bennett profiles  $1/[1 + s^2/S_0^2]^2$  for the density and pressure deviation from ambient

were used in these calculations. The dots (•) on the two curves show the location and spacing (1 mm) of the finite difference grid points in the vicinity of the channel centers.

To compute the vorticity approximately we used the relation

$$\begin{aligned}\bar{V}(t) &= \iint \xi_z dx dy = \int_{-\infty}^{\infty} v_x(x, 0, t) dx \\ &= \int_{x_{\min}}^{x_{\max}} v_x(x, 0, t) dx\end{aligned}\quad (44)$$

where  $x_{\min}$  and  $x_{\max}$  are the respective limits of the coordinates on our grid. To derive Eq. (44) we have assumed that  $v_x, v_y \rightarrow 0$  as  $x, y \rightarrow \infty$ .

Figure 11 shows the results of our calculations of  $\bar{V}(t)$  for  $R_0 = 0.4$ ,  $S_0 = 1.0$ , and  $X_0 = 1.0$  cm using the density profile of the channel formed by the first pulse and the pressure profile of the second pulse as shown in Fig. 10. After an initial positive transient, the integrated vorticity settles down to a steady state negative value after a weak relaxation oscillation.

In deriving Eq. (27) from Eq. (25) the time derivative term  $\frac{\partial v}{\partial t}$ , which must integrate to zero during the expansion, is neglected in favor of the  $v \frac{\partial v}{\partial r}$  term which is always of the same sign and hence contributes most to the integral. A posteriori justification for this approximation is obtained from Fig. 11 which shows the general cancellation of a big transient component in  $\bar{V}(t)$ , as assumed in Section III, and good quantitative agreement with the residual secular term. This means that the amount of vorticity generated depends strongly on the eventual radial displacement of each fluid element but not on the detailed expansion history. The scale of vorticity is set by an average expansion velocity only.

Figure 12 shows a schematic diagram to explain physically how the initial positive vorticity spike of Fig. 11 occurs. The expanding shock, shown at four different times as a dashed line, travels faster and drives the post shock flow faster in the low density material. The density gradient is shown here localized between the two solid semi-circles in an annulus centered at  $S_0$ . The shear resulting from the differential acceleration of the inner and the outer fluid corresponds to vorticity of positive sign which

vanishes, as assumed, when differential velocity ceases. The angle between  $\nabla p$  and  $\nabla P$  (assumed normal to the dashed line shock fronts) is shown at three locations along the original channel periphery. The residual vorticity, which corresponds to that appearing in Eqs. (27) and (30), in effect measures the net outward expansion of the new channel.

Figures 13 and 14 show the vorticity strength  $\bar{V}(t)$  as a function of  $X_0$  with the other remaining variables in our standard case held constant. When the axis of the second pulse fell within  $S_0$  of the center of the channel (Fig. 13), the transient term appeared to oscillate more rapidly than the cases for which the axis of the second pulse fell "outside" the original channel (Fig. 14). The residual values  $\bar{V}(t)$  to which the integrated vorticities in Fig. 13 related were also more nearly equal than in Fig. 14. The general trend of  $\bar{V}(t \rightarrow \infty)$  in the five cases of Figs. 13 and 14 follows qualitatively the shape of  $f_2(a,b,c)$  plotted for various cases in Figs. 4, 5, and 6. The uncanceled vorticity, which we called  $\bar{V}(\tau)$  in Section III, decreases from a maximum around  $X_0 = S_0$  both as  $X_0 \rightarrow 0$  and as  $X_0$  gets large compared to  $S_0$ . The ratio of  $\bar{V}(\tau)$  at  $X_0 = 0.2$  cm to  $\bar{V}(\tau)$  at  $X_0 = 0.1$  cm is probably not as small as expected from the curves of  $f_2$  in Fig. 5 because the sound speed is higher when the second pulse is near the center of the first channel. This increasing sound speed partially counterbalances the tendency of  $f_2$  to fall off as  $X_0$  approaches zero.

The major issue in interpreting these calculations using the formulae of Section III revolves around the choice of  $\frac{U_m^2 \tau}{2}$  for Eq. (30). For Eq. (31) and later estimates we have assumed  $U_m$  is the sound speed of the fluid at the second pulse center before the second pulse is laid down. We have also assumed that the average expansion velocity is  $U_m/2$ .

Figure 15 compares the effects of initial pulse size on the second pulse with the same values of the channel parameters and the overpressure and displacement  $X_0$  of the second pulse. We notice that the transient term appears to scale in magnitude as  $R_0$  while the value of the "residual" vorticity appears to scale as  $R_0^2$ . We may explain the scaling of the residual vorticity in terms of our analytic "late time" treatment. Instead of using the estimate

$$U_m = c_s, \quad (45)$$

as in Eq. (31), we may calculate  $U_m$  from the equation

$$U_m = \frac{2(R_1 - R_0)}{\tau}, \quad (46)$$

where  $\tau$  is the time of expansion from  $R_0$  to  $R_1$ . In Fig. 15, we see that the extrema in  $\bar{V}$  for the cases  $R_0 = 0.2$  cm and 0.4 cm occur at almost the same values of  $t$  and that the relaxation to the final value of  $\bar{V}$  occurs at the same rate for the two cases. Thus we have (for any consistent definition of  $\tau$ ) the relation

$$\tau_A \approx \tau_B. \quad (47)$$

However we expect that

$$R_{1A} \approx \frac{1}{2} R_{1B} \quad (48)$$

since

$$R_{0A} = \frac{1}{2} R_{0B}. \quad (49)$$

Thus Eq. (46) yields

$$U_{mA} \approx \frac{1}{2} U_{mB}. \quad (50)$$

Estimates of the form factor indicate that

$$f_{2A} \approx f_{2B}. \quad (51)$$

Using Eqs. (31) and (46)-(51), we find that

$$\frac{\bar{V}_A(\tau)}{\bar{V}_B(\tau)} \approx \frac{(R_{1A} - R_{0A})^2}{(R_{1B} - R_{0B})^2} \approx \frac{1}{4} \quad (52)$$

for the case shown in Fig. 15.

This analysis indicates that Eq. (45) provides only a crude estimate of  $U_m$  as the energy deposited becomes small. Clearly the relaxation time of the transients depends as much on the already existing density gradients as it does on the new channel expansion laid down. The ambient sound speed at  $X_0 = 1.0$  cm is about  $4 \times 10^4$  cm/sec for the standard case and the reduced energy case of Fig. 15. The final relaxation to the long-time value  $\bar{V}(\tau)$  begins at about 40  $\mu$ sec for both cases, about the time it



takes a sound wave to reach the far side of the original hot channel from the edge of the second pulse (a distance of 1.8 cm and 1.6 cm for cases A and B respectively).

Clearly additional work is required to refine the approximation of Eq. (31), to improve the rather cavalier way in which  $U_m$  has been determined. We expect to carry this study forward in a future report using cases for analysis and simulation which are of prime experimental interest.

In Table I and Fig. 16, we present estimates of the form factor  $f_2$  for the case  $S_0 = 1.0$  cm,  $R_0 = 0.4$  cm,  $R_1 = 1.4$  cm,  $\rho_\infty/\rho_0 = 10$  (channel formed by first pulse) and  $P_\infty/P_0 \approx 31$  (second pulse), as shown in Figs. 7 and 10. These values correspond to  $a \approx 0.4$  and  $b \approx 1.0$ . We vary  $c$  from 0.2 to 2.0. To estimate the value of  $U_m$ , we used Eqs. (45) and (46). For Eq. (46), we define  $\tau$  to be the time elapsed between the deposition of the second pulse ( $t = 0$  in Figs. 13 and 14) and the last extremum in  $\bar{V}(t)$  before the monotonic relaxation to the residual value. The solid curve is the estimate from Eq. (32).

For both methods of estimating  $U_m$  the values of  $f_2$  appear to be somewhat low near  $c = 1.0$ , as we see from comparison of the simulation data points with the analytic calculations also shown in Fig. 16 for the Bennett profile, which was used in our simulations. Here Eq. (45) appears to provide a better estimate of  $U_m$  than does Eq. (46), at least when  $R_0 = 1.0$  cm. Better agreement is expected when the energy deposition is slow and the adiabatic expansion treatment is a better approximation.

Finally, returning to Fig. 1, assume  $U_m \approx 2.0 \times 10^4$  cm/sec,  $R_1 - R_0 \approx 15\%$  of 4 mm = 0.06 cm,  $\ln(\rho_\infty/\rho_0) \approx 0.33$ , and choose  $f_1 = -1/20$  for a smaller relative displacement than shown in Fig. 3. The expansion velocity is smaller here because the pulse is weak. The predicted value of  $\bar{V}(\tau)$  is 20 cm<sup>2</sup>/sec. The corresponding mixing time is about 60 msec for two pulses and perhaps a half or a third of that time if the vorticity from the subsequent third and fourth pulses add roughly linearly. More accurate estimates for these data, kindly provided by the authors,<sup>2</sup> must await specific detailed calculations in a future publication.

## V. SUMMARY AND CONCLUSIONS

Formulae have been developed and calibrated for calculating the integrated vorticity and subsequent convective mixing time resulting after a second circular heating pulse is injected parallel to the axis but off center in a hot channel created by an earlier pulse. The vorticity arises because the density gradient asymmetries interact with pressure gradients attendant on the second heating pulse. Two oppositely rotating vortex filaments give rise to a shearing, mixing flow field which tends to convect the original channel toward the center of the second pulse.

The following formulae summarize the results of this paper. Assume a hot channel exists with a central density  $\rho_0$  lower than ambient density  $\rho_\infty$  and with a characteristic radius  $S_0$  for the density variation. In the simulations performed for this paper a Bennett profile was used:

$$\rho(s) = \rho_\infty - \frac{(\rho_\infty - \rho_0)}{[1 + (s/S_0)^2]^2} \quad (53)$$

both for the original channel and for the subsequent energy depositions. A second pulse is deposited a distance  $X_0$  off center in the heated channel with an overpressure  $\delta P_{\max}$  at the center and a characteristic radius  $R_0$ .

$$P(r) = P_\infty + \frac{\delta P_{\max}}{[1 + (r/R_0)^2]^2} \quad (54)$$

for the simulations reported here. The extra energy deposited per unit length by this second pulse is

$$\Delta E = \frac{\pi R_0^2 \delta P_{\max}}{(\gamma - 1)} \quad (55)$$

which may also be used to calculate  $\delta P_{\max}$  from  $\Delta E$ . For the calculations reported here  $\delta P_{\max} = 30$  and  $R_0 = 0.4$  cm (generally).

If adiabatic expansion of the second pulse channel to ambient pressure is an adequate approximation as suggested by Lampe,<sup>3,7</sup> the final characteristic radius of the expanded pulse channel will be (approximately)

$$R_1 \approx R_0 \left[ \frac{\delta P_{\max}}{P_{\infty}} + 1 \right]^{\frac{1}{2\gamma}}. \quad (56)$$

Giving  $R_1 - R_0$  for use in Eq. (31). The integrated vorticity in each of the two filaments,  $\pm \bar{V}(\tau)$ , is given adequately by the formula

$$\bar{V}(\tau) \approx c_s(X_0)(R_1 - R_0) \ln \left( \frac{\rho_{\infty}}{\rho_0} \right) f_2 \left( \frac{R_0}{R_m}, \frac{R_m}{S_0}, \frac{X_0}{S_0} \right) \quad (57)$$

where the sound speed  $c_s(X_0)$  is evaluated in the original channel at the location where the second pulse will be centered. The radius  $R_m$  lies between  $R_0$  and  $R_1$  and we have taken it to be 1.0 cm when  $R_0 = 0.4$  cm and  $\delta P_{\max} = 30$ . If the original channel overpressure is  $\delta P_{\max}^*$ ,  $\rho_{\infty}/\rho_0$  is given by an expression analogous to Eq. (56)

$$(\rho_{\infty}/\rho_0) = \left[ \frac{\delta P_{\max}^*}{P_{\infty}} + 1 \right]^{\frac{1}{\gamma}}. \quad (58)$$

The geometric form factor  $f_2(a, b, c)$  is given by the simple quadrature

$$f_2(a, b, c) = \int_a^{\infty} \eta d\eta \frac{[g(S_0[\eta b + c]) - g(S_0[\eta b - c])]}{[1 + \eta^2 - a^2]^2} \quad (59)$$

where the original channel density satisfies

$$\rho(s) = \rho_{\infty} e^{-\ln \left( \frac{\rho_{\infty}}{\rho_0} \right) g(s/S_0)}. \quad (60)$$

Equation (59) for the form factor is a permissible simplification when  $g(s/S_0)$  is expressible in even powers of  $s$ . Plots of this form factor for a number of cases are presented in Figs. 4, 5, 6 and 16. It typically takes on negative values with an extremum of  $f_2 \approx -\frac{1}{3}$  in the vicinity of  $X_0 = S_0$  ( $c = 1$ ) and approaches zero for both large and small values of  $X_0$ .

Using Eq. (57) for the generated vorticity, a mixing time estimate can be derived as in Section II,

$$\tau_{\text{mix}} \approx \frac{\sqrt{6} \pi S_0^2}{|\bar{V}(\tau)|}. \quad (61)$$

This is the time it takes cold fluid from one side of the original channel to cross the hot region and reach the other side—thus effectively bisecting the hot channel with cool fluid. The negative sign on  $f_2$  means physically that the vortex-induced cold jet moves toward and into the second pulse channel rather than away from it.

As an example of the use of these formulae, consider the case of  $\Delta E$  ergs/cm being deposited by each pulse in a cylinder of initial radius  $R_0$ . The overpressure factor is

$$\Gamma \equiv \frac{\delta P_{\max}}{P_{\infty}} = \frac{(\gamma - 1) \Delta E}{\pi R_0^2 P_{\infty}} \quad (62)$$

and the mixing time estimate of Eq. (61) can then be written

$$\tau_{\text{mix}} = \frac{R_0}{U_T} \frac{(1 + \Gamma)^{\frac{1}{\gamma}}}{[(1 + \Gamma)^{\frac{1}{2\gamma}} - 1] \ln(1 + \Gamma)} \quad (63)$$

The typical turbulence velocity  $U_T$  is given by the expression

$$U_T = \frac{\langle f_2 \rangle c_s(X_0)}{\sqrt{6\pi\gamma}} \approx 10^3 \text{ cm/sec} \quad (64)$$

where the value of  $10^3$  cm/sec assumes  $\langle f_2 \rangle c_s \sim 10^4$  cm/sec. Since  $c_s \sim 5 \times 10^4$  cm/sec and  $|f_2| \sim \frac{1}{5}$  in the range  $0.5 S_0 \leq X_0 \leq 1.5 S_0$ , this is a good approximation.

A single curve, as seen from Eq. (63), serves to characterize the non-dimensional vorticity mixing time in terms of the instantaneous pulse overpressure. However, since  $\delta P_{\max}/P_{\infty}$  also depends on  $R_0$ , curves of  $\tau_{\text{mix}}$  for several values of  $R_0$  are plotted in Fig. 17. For tightly focused beams ( $R_0$  small and  $\xi$  large) the mixing times are very fast so convective/turbulent cooling is bound to play a significant role in multipulse propagation. Overpressures significantly less than unity must be used with pulses separated by  $10^{-3}$  sec or more when the beam radius is 1 mm. In fact mixing will significantly alter channel dynamics with a deposition radius of 1 mm and overpressure of 10 unless the pulse separation in time is reduced well below 100  $\mu$ sec.

There is much still to be learned about this vorticity generation mechanism which may have a telling role in determining overall channel coding characteristics. In closing this paper it is appropriate to identify several of these issues which appear to play a major role and which have been dealt with only approximately above. Where possible the likely effect is described and discussed.

In our theoretical model for the integrated vorticity, a great simplification was achieved by evaluating the integrand at a point in time when the maximum expansion velocity was attained and then replacing  $U_m^2 \frac{\tau}{2}$  with  $c_s(R_1 - R_0)$ . For moderate strength shocks this should work reasonably well. Ignoring for now the question of what is the "correct" average to take, it should be clear that the formula is probably wrong for both very strong energy deposition and for relatively weak energy depositions. Strong shocks leave large yet subsonic velocities in their wakes. In terms of the ambient sound speed (at the pulse location), this velocity of expansion may be quite supersonic making our approximation actually underestimate the vorticity generated. On the other hand, for weaker energy depositions the shock speed is still slightly larger than  $c_s$  but the flow speed, and hence the expansion rate, can be much smaller.

These weaker cases may well be treated as dynamic adiabatic expansions where  $R_1/R_0 - 1$  is small but detailed numerical simulations will be needed to calibrate the improved theoretical model. It may well be that the effective expansion time  $\tau$  and hence the effective expansion velocity  $\frac{U_m}{2}$  should involve the maximum of the shock transit time from  $R_1$  to  $R_0$  and the rarefaction wave transit time to the axis from  $R_0$ . The effect of reducing the vorticity generation rate at low deposition power means that there will probably be a shift of the least mixed channel to larger size since not only  $R_1 - R_0$  but also the effective expansion velocity  $\frac{U_m}{2}$  decrease when the overpressure  $\Gamma$  is small.

In reality the energy deposition will probably depend on the existing channel profiles. Lower density often means reduced energy deposition although perhaps equal or near equal local heating may result. Furthermore, circular energy deposition will no longer apply. While it may not yet be possible

to evaluate the channel effect on subsequent pulse propagation, the effect on the channel of an energy deposition with given cross section should be easier to determine. It will be particularly important to characterize these phenomena quantitatively because a reduction in the beam-generated turbulence is likely. This in turn reduces the turbulence level and hence convective channel cooling. For near term experiments these refinements and the corresponding reduced cooling for low intensity beams will probably help raise the average channel temperature. For more intense beams, the turbulence problem may well be worse than we predict here because  $\frac{U_m}{2}$  may be larger than  $c_s$ .

Distortion of either a two-dimensional or a three-dimensional variety will also contribute to the vorticity and hence turbulence generation. These additional asymmetries must also be analyzed theoretically. Even in the initially 2D cases three-dimensional effects are likely to appear and reach full amplitude by the time an averaged description of the "turbulent" channel cooling will become useful. This is not likely to occur before a few pulses at least so the use of detailed (and probably expensive) calculations is necessary to bridge the gap between a single pulse interacting with a previously bored smooth channel and a roughly circular turbulent cylinder being driven by a repetitively pulsed energy source near its axis.

Questions about the vorticity generation in highly distorted geometries must be resolved. As the symmetry plane jet develops in the simplest case, the hot, double channel becomes bisected into two channels with embedded vorticity. A third pulse might be expected to bisect these two channels—if the location and timing of the pulse were correct. It is clear that the timing is important because the vorticity should add essentially linearly when the pulses are separated by a time appreciably shorter than the mixing time estimated above. By separating the pulses sufficiently in time, on the other hand, interesting nonlinear effects will result. Proper phasing and location of the pulses can certainly cancel existing vorticity in some regions and enhance it in others.

As the number of pulses increases so also will the geometric complexity of the resulting composite channel. A turbulent situation is expected to result in which the migrating, interacting vortex

filaments shear and stir the hot expansion channels. This mixing brings cold entrained air into proximity with the hot channel air on spatial scales short compared to an expanded channel radius and thus molecular thermal conduction cooling is expected to be enhanced. Questions in the turbulence regimes occur at a number of points. Where the beam-generated vorticity goes and how it evolves are clearly controlling issues. The same reduction of scales by the expansion induced jets which tends to favor enhanced molecular thermal conduction will also favor enhanced viscous dissipation of the driving vortices themselves. Since the decay of vorticity reduces the convective cooling rate, a balance will be obtained eventually where the production of vorticity is equal to the dissipation rate.

In standard turbulence phenomenologies there is no good way for dealing with transient, multispace-scale phenomena so a model for these effects will have to be developed which also allows the complex channel to be cooler, on average, at the edges than in the center. The importance of temperature fluctuations also cannot be overemphasized. Knowing the average channel temperature is not sufficient if one very hot region takes on unusual importance. Thus a transient turbulence model will also have to be constructed which allows molecular cooling so the temperature fluctuations about the mean can be analyzed.

Work is currently underway to extend this analysis to the other types of asymmetry and to perform detailed simulations of the late time channel cooling to calibrate the mixing time formula as well as the vorticity generation formula. Three-dimensional simulations of the early time and the development of a spectral dynamics turbulence phenomenology for the late time will be necessary before a truly interactive multipulse scenario can be simulated where the beam deposition-vorticity generation-channel distortion feedback loop is incorporated. A framework for the turbulence analysis has been developed, and will serve as the basis for our improved analysis of these issues in future research.

## ACKNOWLEDGMENT

The authors would like to acknowledge helpful conversations with M. Lampe, D. Book, T. Fessendon, and S. Yu. This work was supported by DARPA under program element NSWC61101E. The FAST2D computer code used to perform these calculations was developed under support from ONR and DNA.

## REFERENCES

1. J.R. Greig, R.E. Pechacek, R.F. Fernsler, I.M. Vitkovitsky, A.W. DeSilva, and D.W. Koopman, "A Preliminary Study of Aerosol Initiated CO<sub>2</sub> Laser Produced Air Sparks and Their Ability to Guide Electrical Discharges", NRL Memorandum Report 3647.  
  
J.R. Greig, D.W. Koopman, R.F. Fernsler, R.E. Pechacek, I.M. Vitkovitsky, and A.W. Ali, "Electrical Discharges Guided by Pulsed CO<sub>2</sub>-Laser Radiation", *Physical Review Letters*, **41**, 174-176 (1978).  
  
D. Koopman, J. Greig, R. Pechacek, A. Ali, I. Vitkovitsky, and R. Fernsler, "CO<sub>2</sub>-Laser Produced Channels for Guiding Long Sparks in Air", *Journal De Physique, Colloque C7, Supplement au n°7*, Tome 40, Juillet 1979, C7-419.  
  
M. Raleigh, J.D. Sethian, L. Allen, J.R. Greig, R.B. Fiorito, and R.F. Fernsler, "Experiments on the Injection of Relativistic Electron Beams into Preformed Channels in the Atmosphere", NRL Memorandum Report 4220.
2. T.J. Fessendon, R.J. Briggs, R.E. Hester, E.J. Lauer, and R.L. Spoerlein, "ASTRON High Pressure Channel Experiments", report nearing completion.
3. M. Lampe, H.H. Szu, and S. Kainer, "Hydrodynamics of Gas Channel Formation," NRL Memo. Report 4073.



NRL MEMORANDUM REPORT 4327

4. J.P. Boris, "Flux-Corrected Transport Modules for Solving Generalized Continuity Equations," NRL Memorandum Report 3237 March 1976.
5. J.P. Boris, "Dynamic Stabilization of the Imploding Shell Rayleigh-Taylor Instability," *Comments on Plasma Physics and Controlled Fusion* (3) No. 1, pp 1-13, 1977.
6. D.L. Book, J.P. Boris, A.L. Kuhl, E.S. Oran, J.M. Picone, and S.T. Zalesak, "Simulation of Complex Shock Reflections from Wedges in Inert and Reactive Gaseous Mixtures," proceedings of Seventh International Conference on Numerical Methods in Fluid Dynamics, June 23-27, 1980, Stanford Univ-NASA Ames, U.S.A.
7. M. Lampe, private communications.

Table I. Values of  $f_2$  from numerical simulations. The displacement of the second pulse from the channel center is varied ( $c \equiv X_0/S_0$ ) and two different estimates of  $U_m$  are compared. The sound speed in the original channel at the second pulse center is indicated.

$c$	$U_m = C_s(X_0)$	$-f_2(C_s)$	$U_m$ (eq.46)	$-f_2$ (eq.46)	$-\bar{V}(\tau)$
0.2	$8.2 \times 10^4 \frac{\text{cm}}{\text{sec}}$	0.10	$8.0 \times 10^4 \frac{\text{cm}}{\text{sec}}$	0.10	$1.9 \times 10^4 \frac{\text{cm}^2}{\text{sec}}$
0.5	$5.2 \times 10^4$	0.18	$6.3 \times 10^4$	0.14	$2.1 \times 10^4$
1.0	$3.9 \times 10^4$	0.23	$5.9 \times 10^4$	0.15	$2.1 \times 10^4$
1.5	$3.6 \times 10^4$	0.19	$4.2 \times 10^4$	0.17	$1.6 \times 10^4$
2.0	$3.5 \times 10^4$	0.15	$3.2 \times 10^4$	0.16	$1.2 \times 10^4$

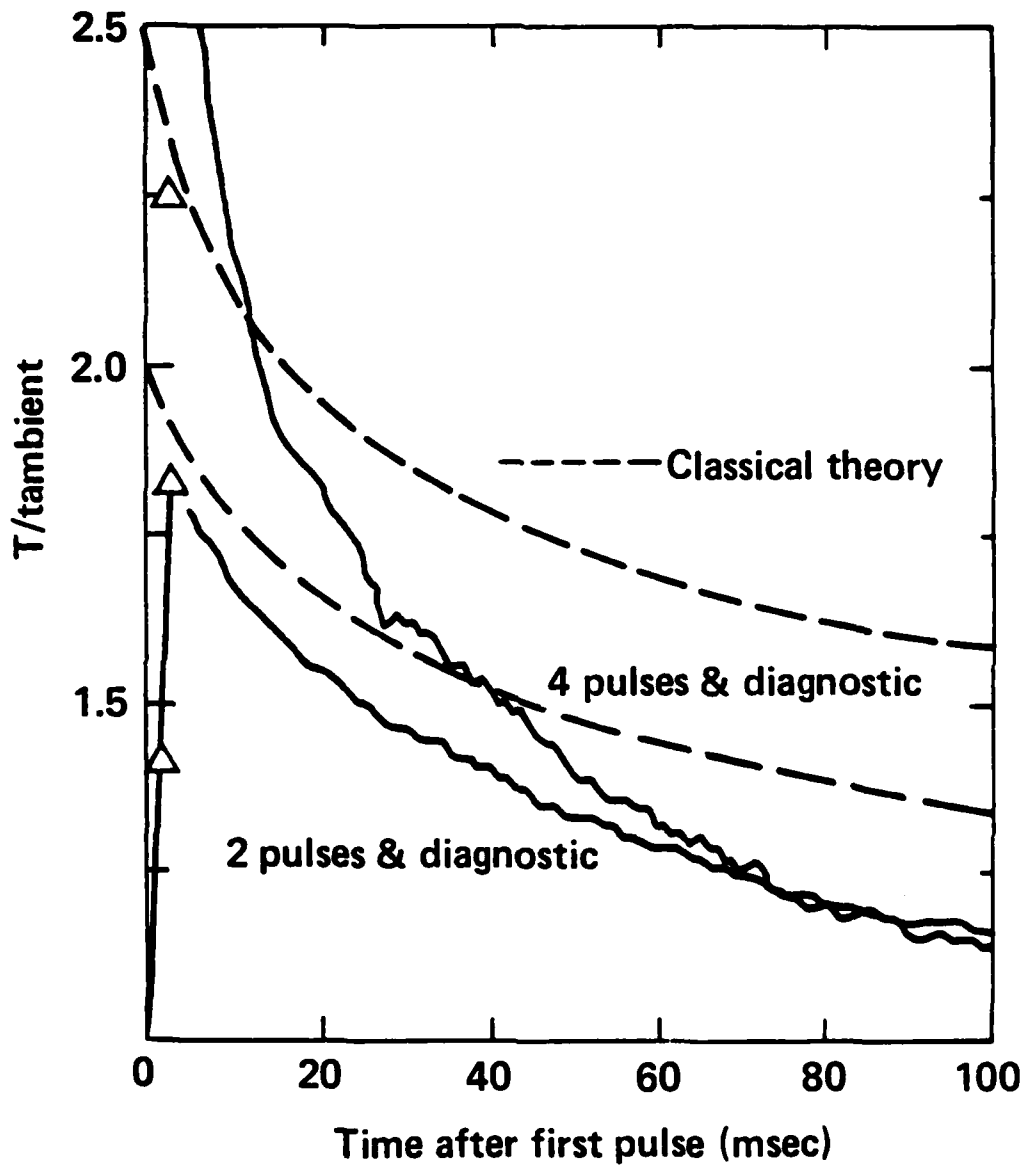


Fig. 1 — Measure of temperature rise versus time for multipulse channel formation using Astron (by permission of the authors). The "classical theory" curve indicates that cooling occurs faster than can be accounted for by thermal conduction alone.

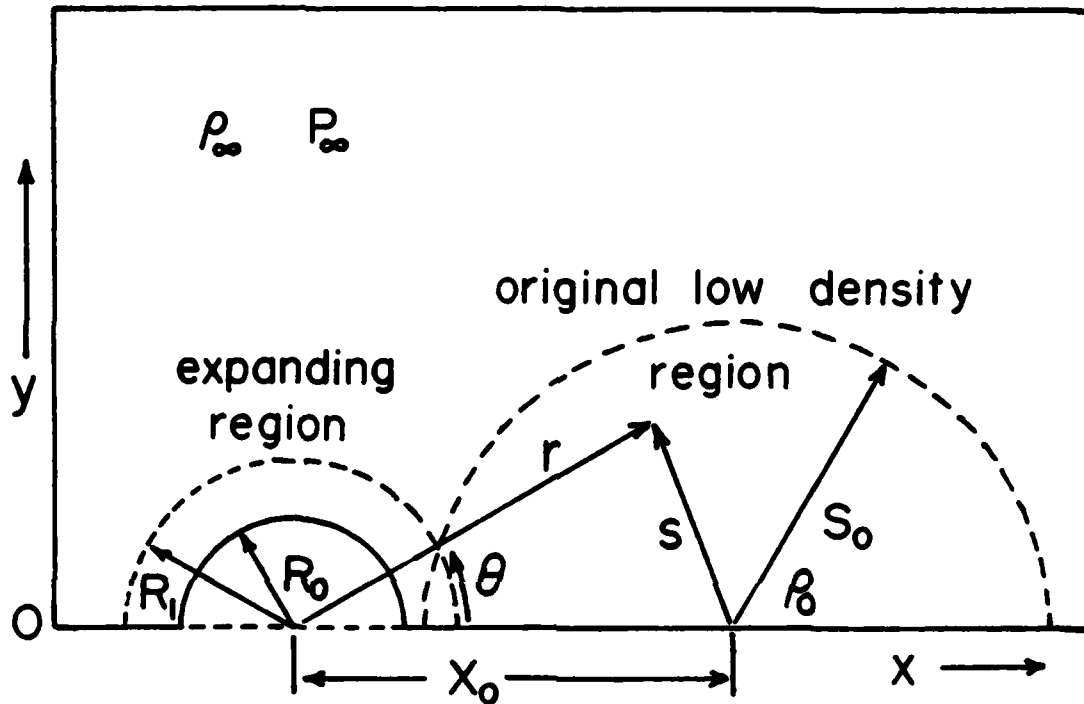
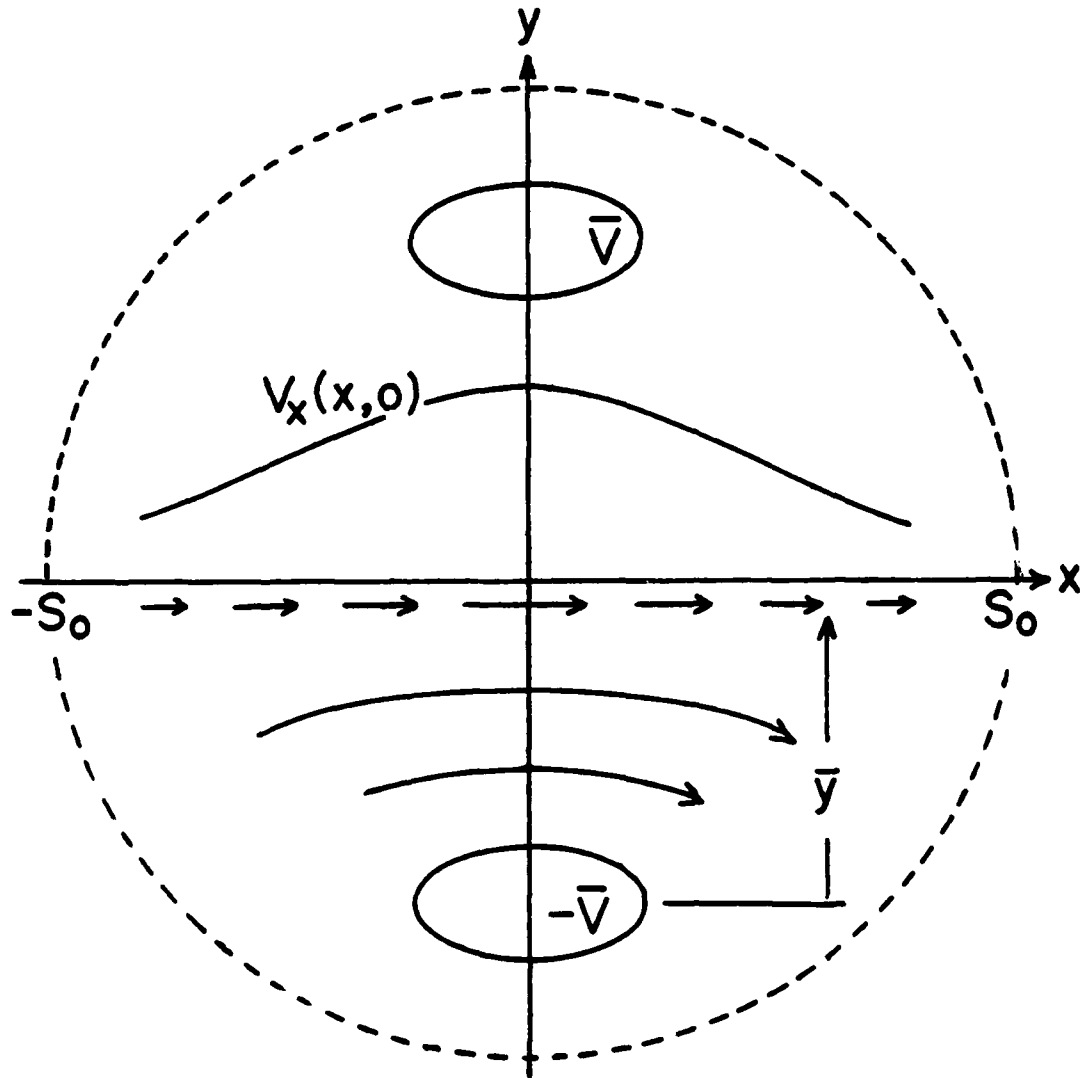


Fig. 2 — Schematic of the initial conditions in which a second beam pulse of radius  $R_0$  propagates parallel to the hot channel of characteristic radius  $S_0$  formed by a previous beam pulse. The second pulse, offset from the first pulse by  $X_0$ , expands to radius  $R_1$ .



$$\tau_{\text{mix}} = \frac{2\pi S_0}{\bar{V} \bar{y}} \left[ S_0^2/3 + \bar{y}^2 \right]$$

Fig. 3 — Symmetric distribution of localized vorticity appears as two extended vortex filaments  $\bar{V}$  separated by a distance  $2\bar{y}$ . Flow velocity induced by these vortices is shown along the  $x$  axis halfway between the filaments. The mixing time  $\tau_{\text{mix}}$  is defined here as the time it takes a fluid element at  $-S_0$  to reach  $S_0$  and hence effectively bisect the hot channel.

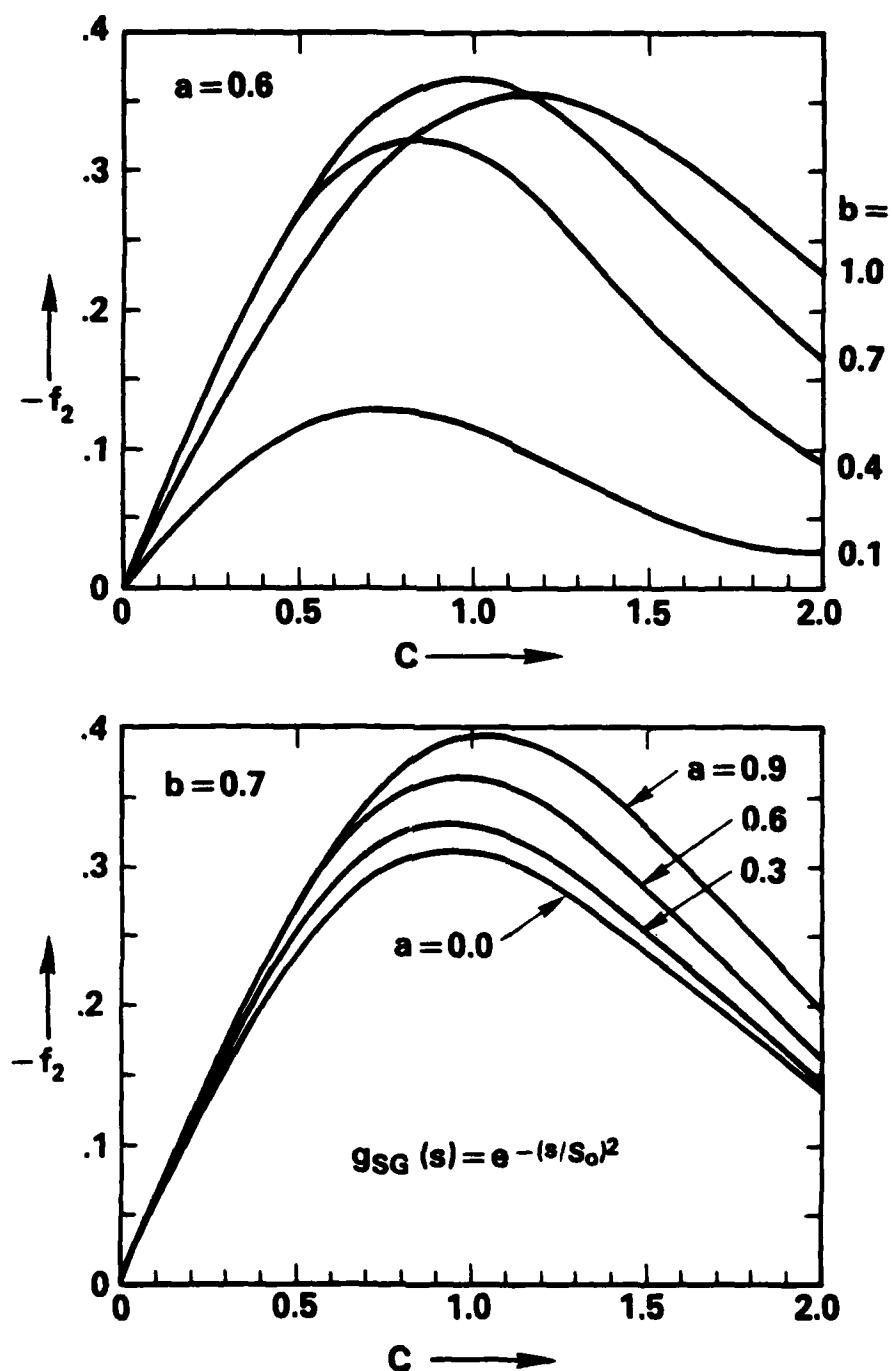


Fig. 4 — Integrated vorticity form factors assuming a "super-Gaussian" density profile. Larger variation with  $b$  is observed in the upper figure than with  $a$  in the lower figure. Peak vorticity generation always seems to occur in the vicinity of  $X_0 = S_0$  and  $-f_2$  ranges from 0.1 to 0.4 in maximum value with 0.3 being a good working value.

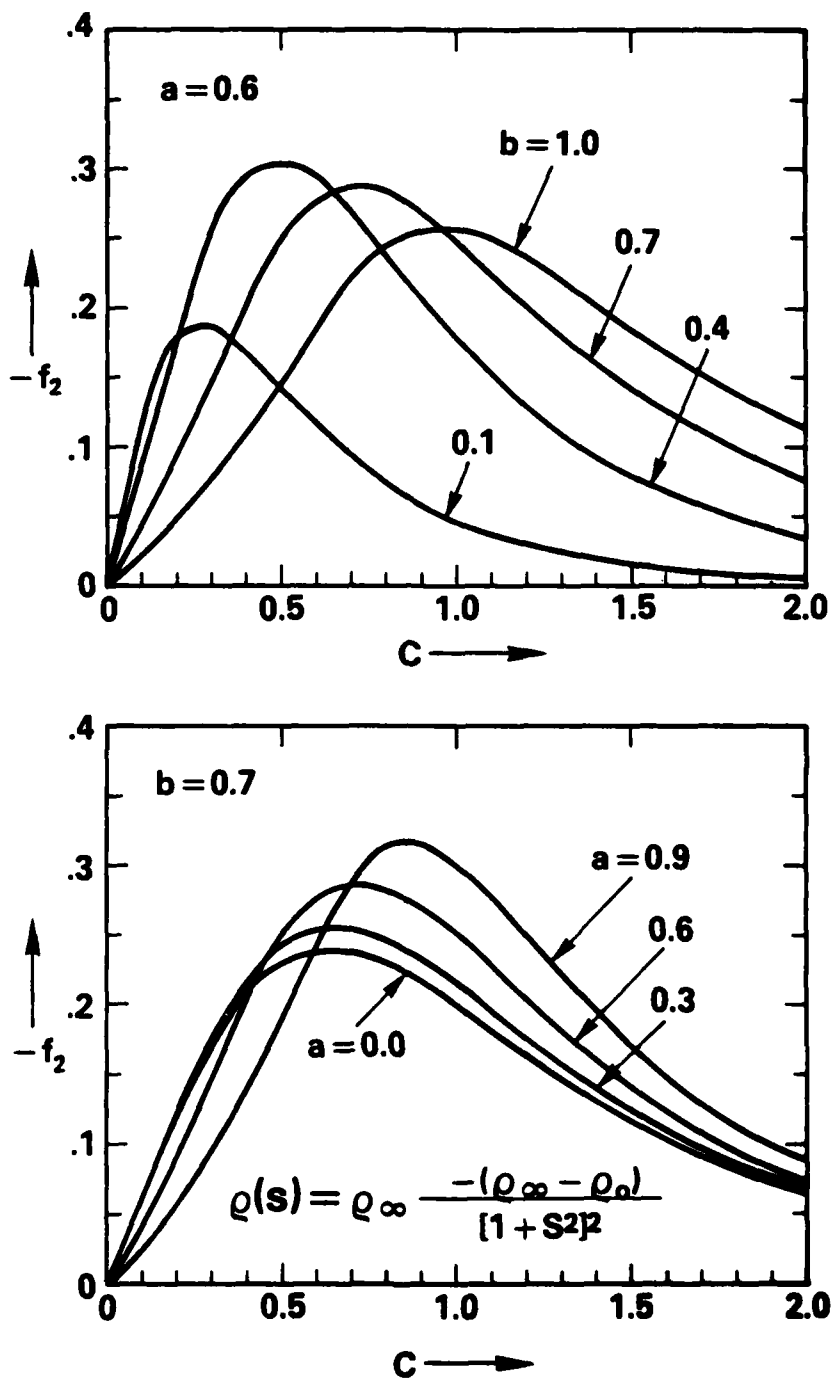


Fig. 5 — Integrated vorticity form factors assuming a Bennett density profile. Larger variation with  $b$  is again observed than with  $a$ . Note that appreciable form factors at  $X_0 \sim 0.2 S_0$  can be obtained when  $b$  is small.

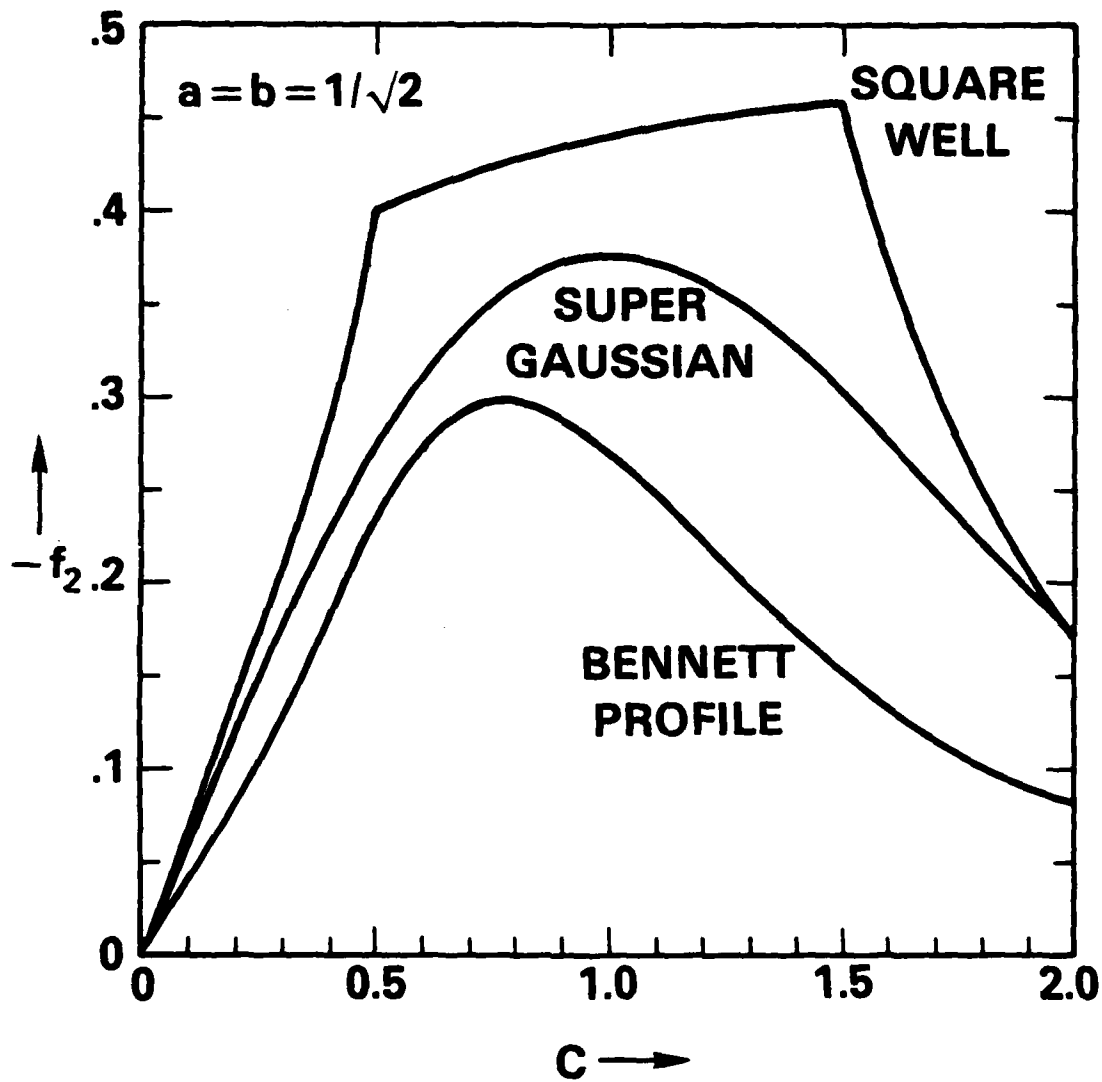


Fig. 6 — Comparison of integrated vorticity form factors for three distinct density profiles at  $a = b = 1/\sqrt{2}$ . Relatively little variation in the form factors is seen for the widely differing density profiles



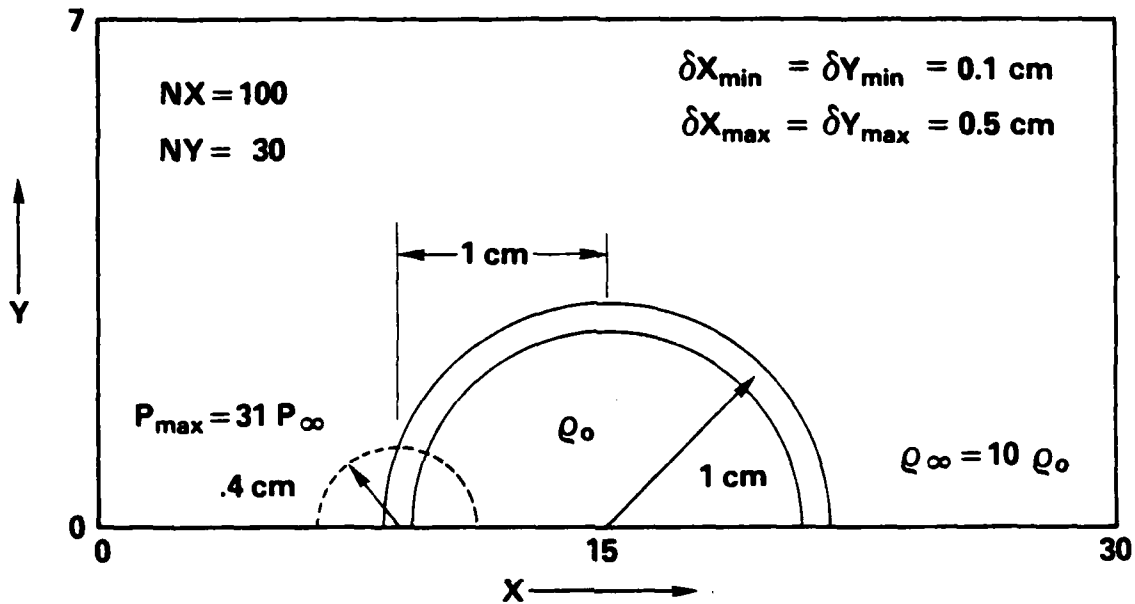


Fig. 7 — Initial conditions for numerical simulations of beam-channel vorticity generation mechanism. Only the upper half plane is simulated with outflow boundary conditions at  $X = 0 \text{ cm}$ ,  $X = 30 \text{ cm}$  and  $y = 7 \text{ cm}$ . A 5:1 grid stretching has been employed for the outermost zones to move the boundaries far from the active region.

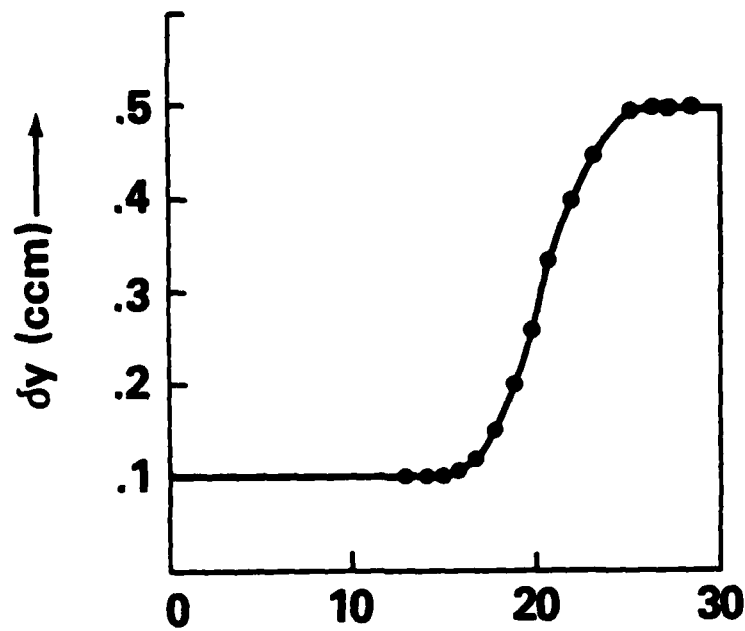


Fig. 8 — Plot of  $\delta y$  versus cell number for the variably spaced  $y$  grid. Adaptive gridding reduces possible boundary reflection of shocks to a small error by putting boundaries of the computational domain far from the hot channel.

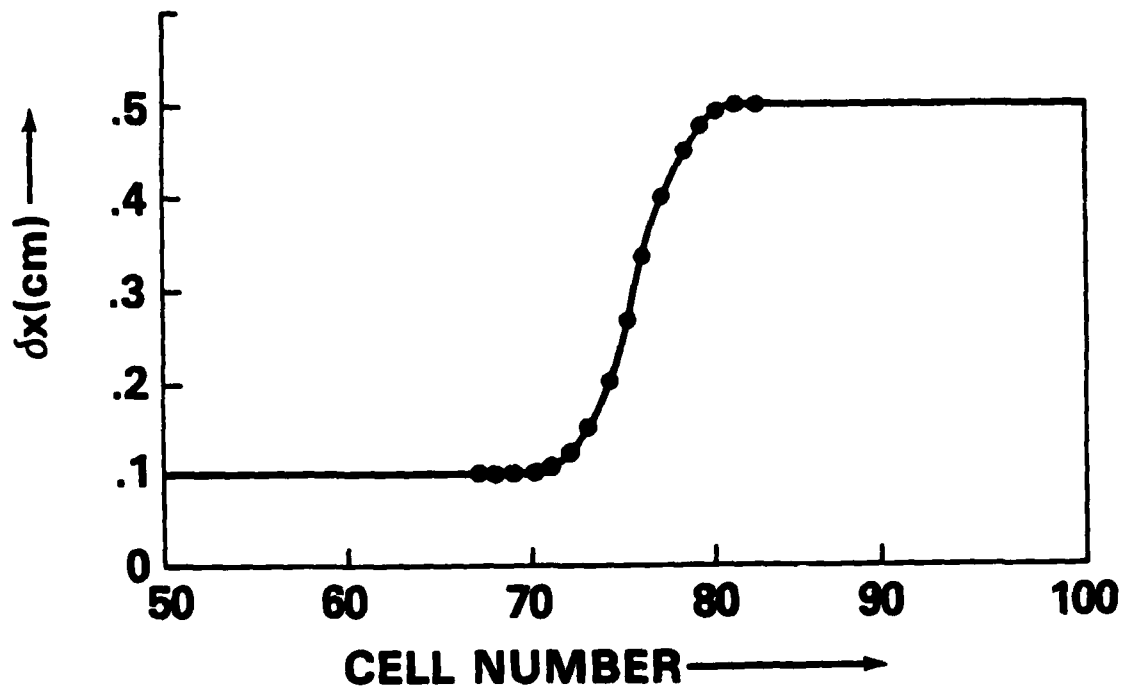


Fig. 9 — Plot of  $\delta x$  versus cell number for the variably spaced  $x$  grid. Only cells 51-100 are shown because the spacing from cell 1 to cell 50 is the mirror image of the spacing from 51 to 100.

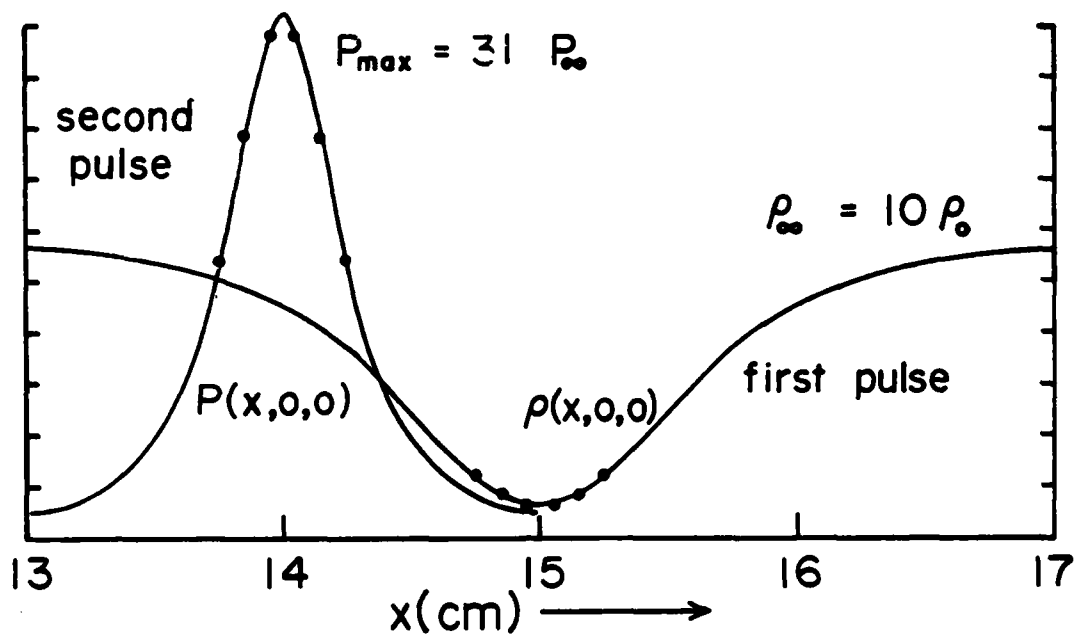


Fig. 10 — Symmetry plane pressure and density profiles for the case where the second pulse and first pulse channel centers are separated by 1.0 cm. The first pulse characteristic channel radius is  $S_0 = 1.0$  cm and the second pulse characteristic channel radius is 0.4 cm (see Figs. 2 and 7). Data points are shown near the channel centers to indicate good resolution used in the fine zone region.

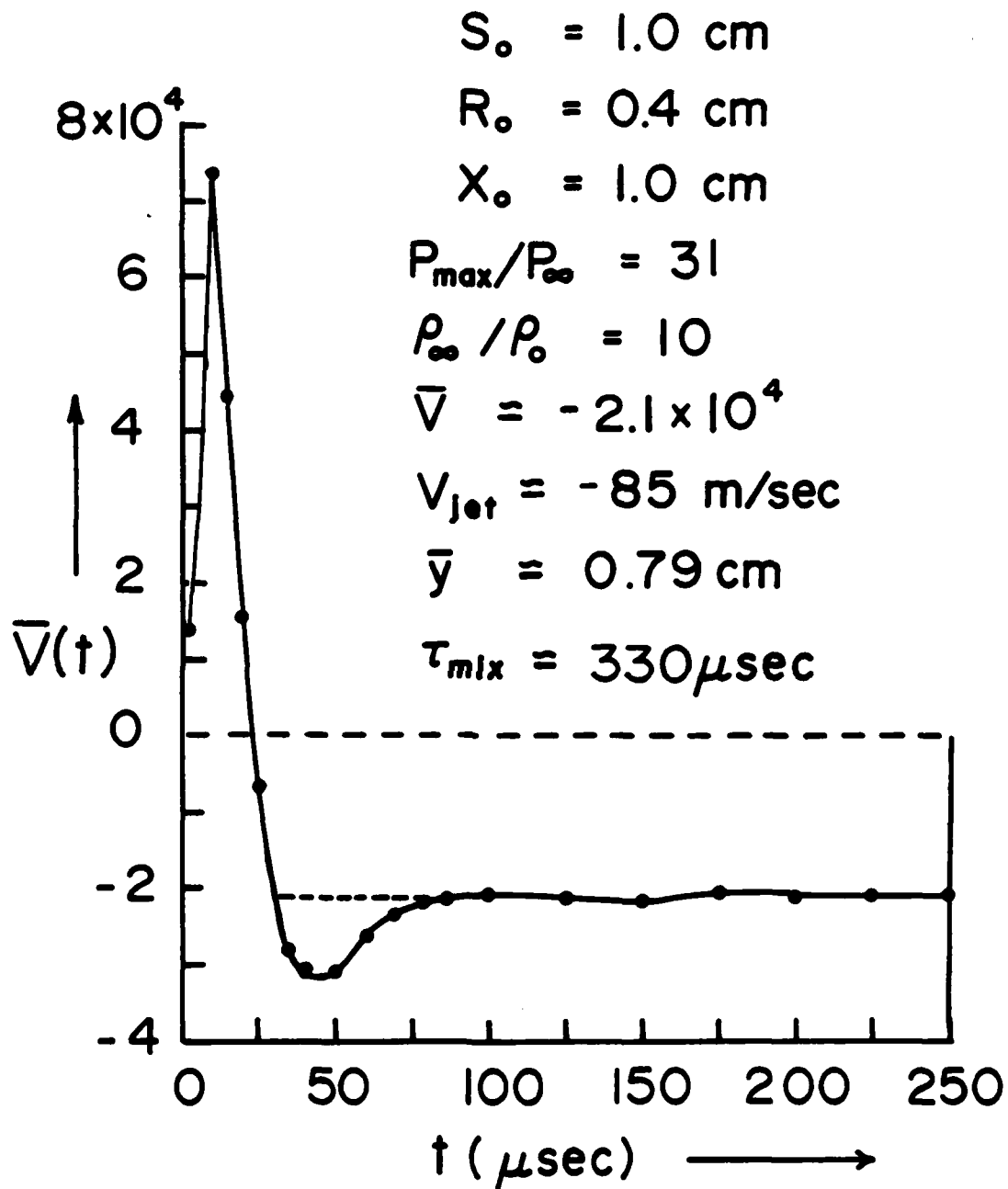


Fig. 11 — Time history of the integrated vorticity in the upper half plane for our standard case. Overall vorticity is zero, of course, because an equal strength but oppositely directed vortex filament is generated in the lower half plane.

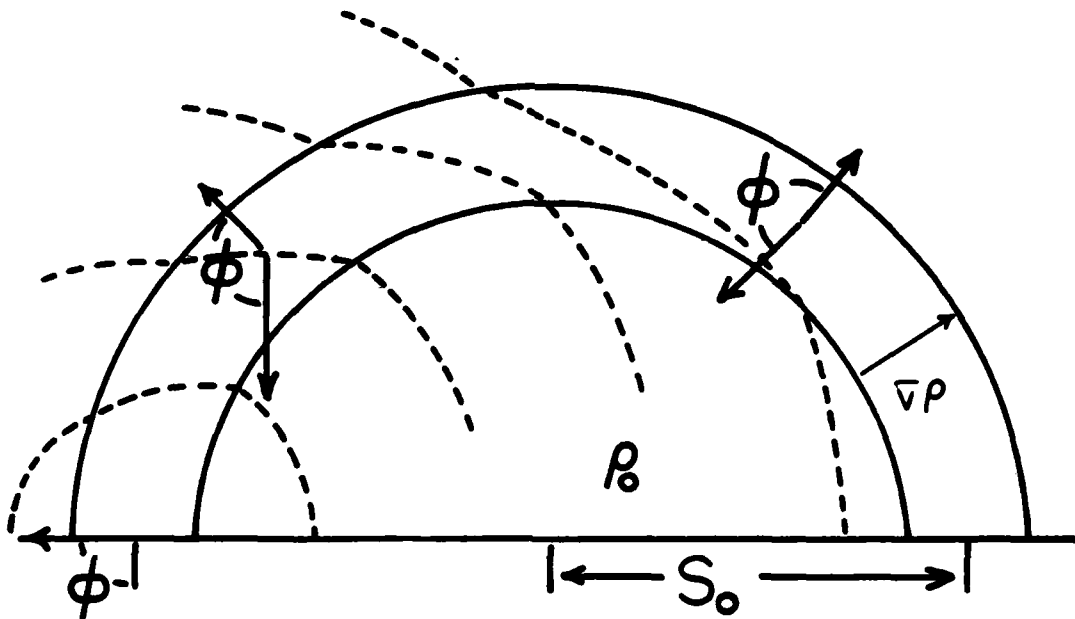


Fig. 12 — Schematic diagram showing how initial vorticity transient arises physically. When the outwardly expanding fluid eventually decelerates to rest, most of the transient vorticity cancels because the acceleration pressure gradient must change sign to stop the expansion.

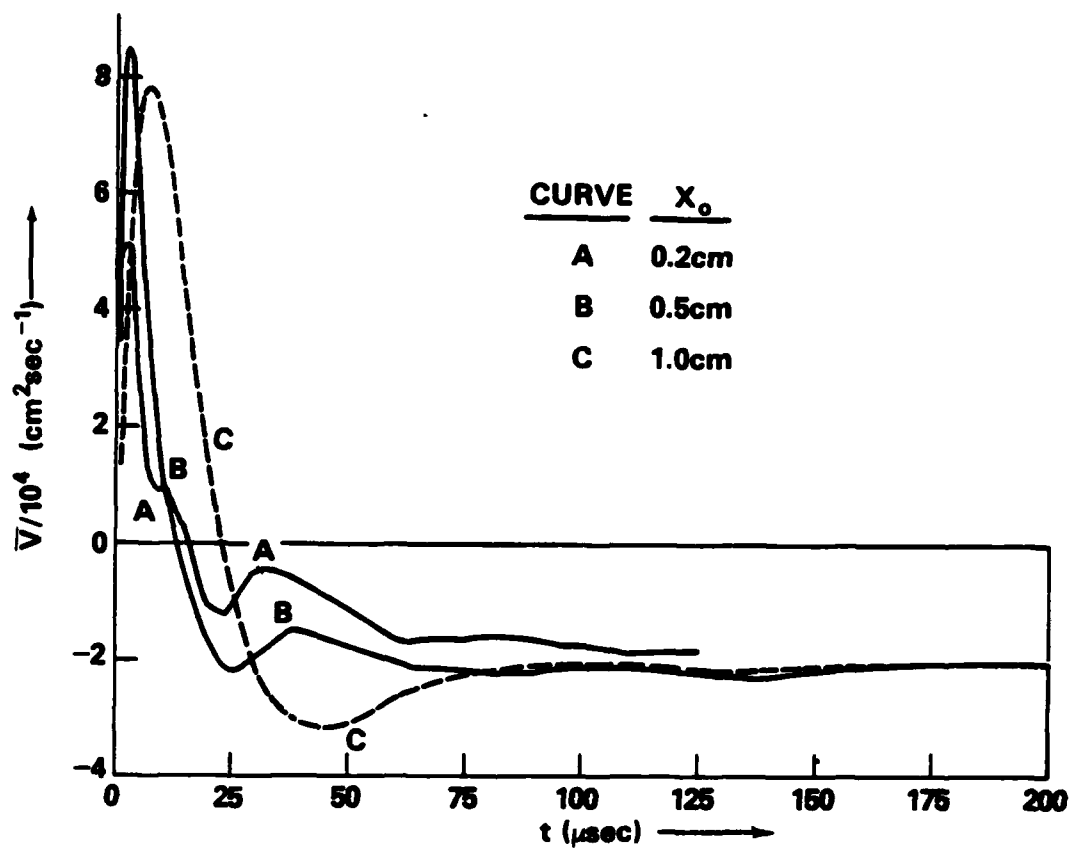


Fig. 13 — Integrated vorticity  $\bar{V}(t)$  for three cases with  $X_0 \leq S_0$ .

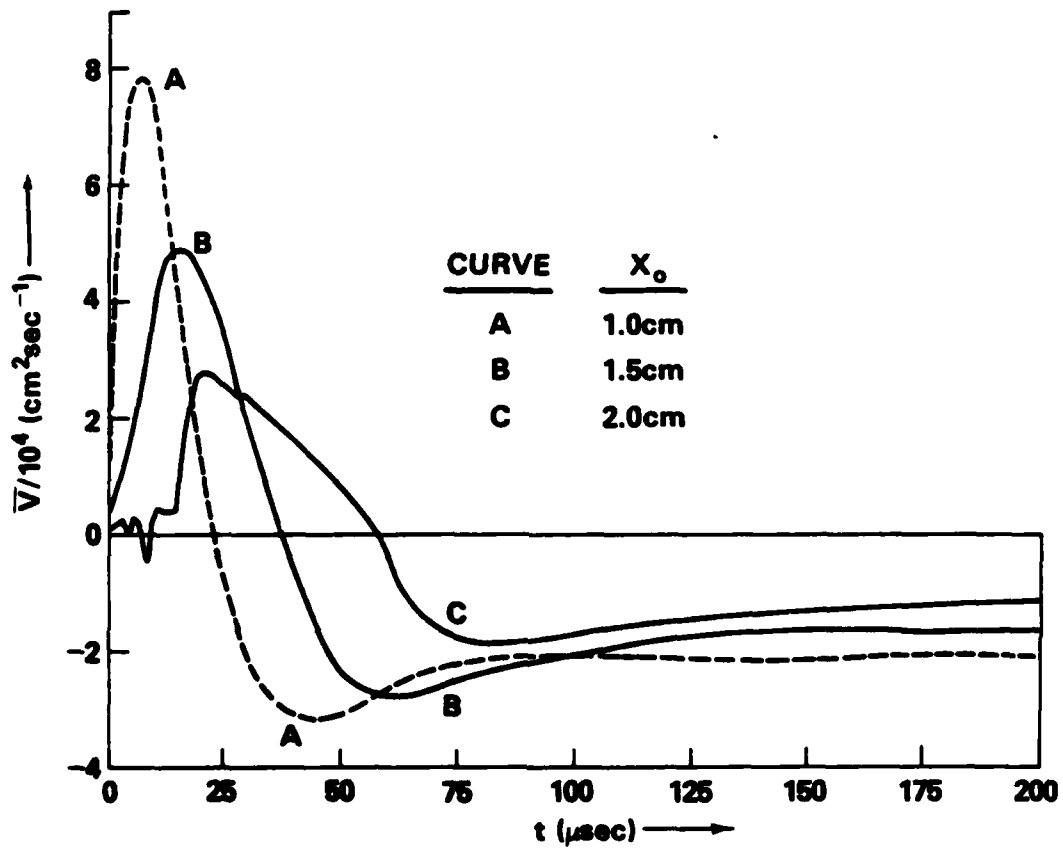


Fig. 14 — Integrated vorticity  $\bar{V}(t)$  for three cases with  $X_0 \geq S_0$ .

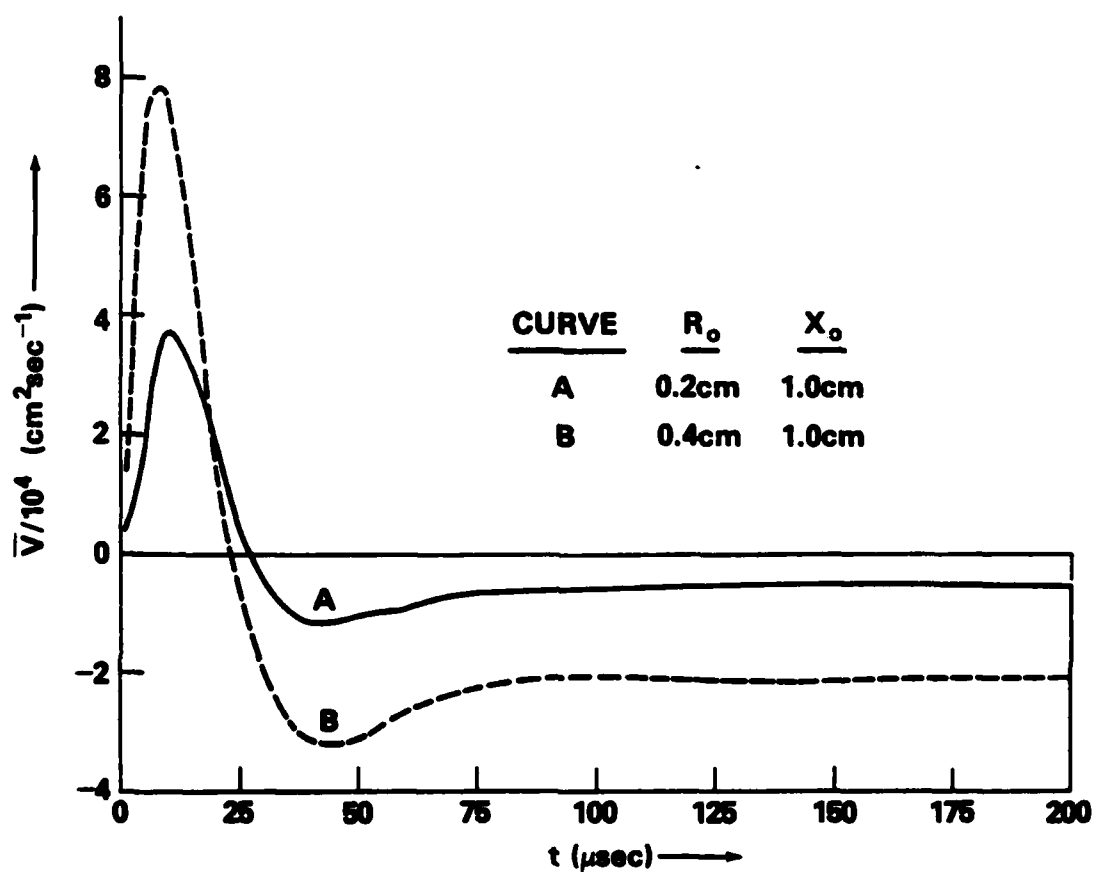


Fig. 15 — Integrated vorticity  $\bar{V}(t)$  for two cases differing only in second pulse radius. Curve B is the standard case and Curve A has one fourth the energy per unit length deposited in one fourth the area so the peak overpressures are equal. The transients differ by a factor of two but the residual integrated vorticity differs by a factor of 4.



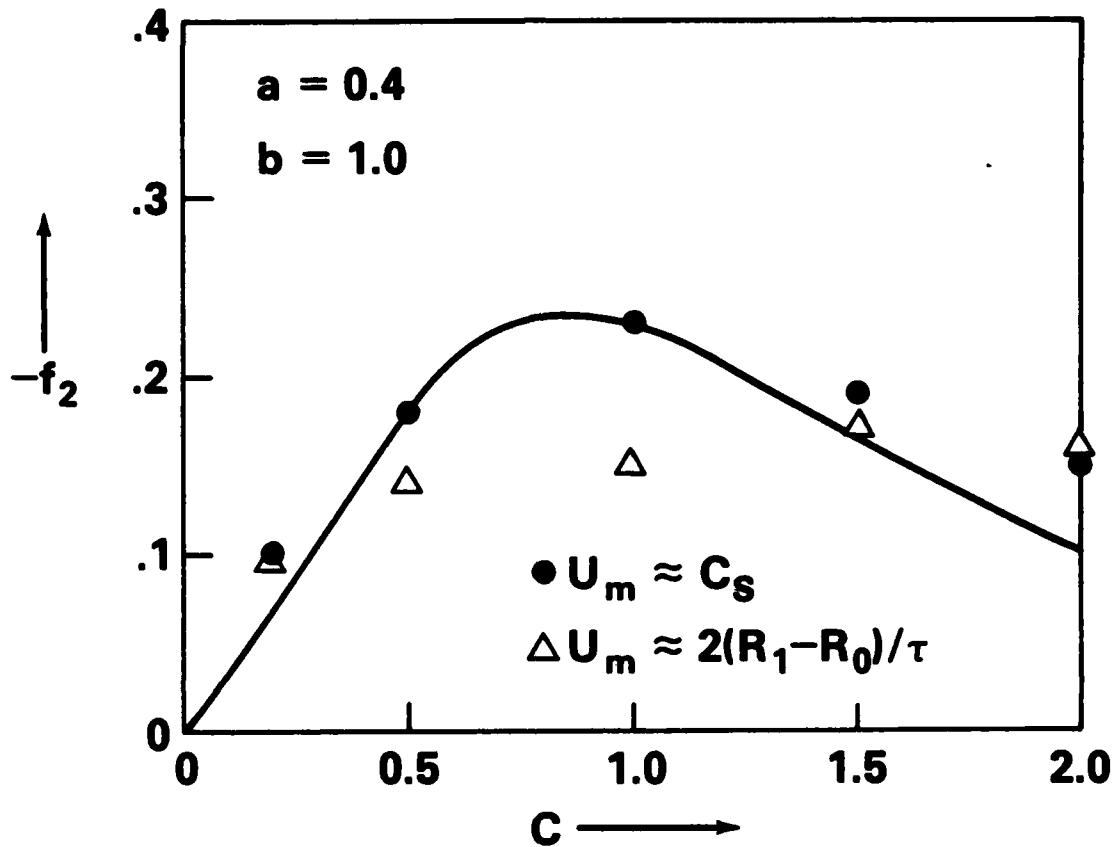


Fig. 16 — Comparison of numerically determined form factors ( $\bullet$  and  $\Delta$ ) with the theoretical calculation using the vorticity generation formulation and setting  $a = 0.4$ ,  $b = 1.0$ . Agreement is good in both magnitude and sign.

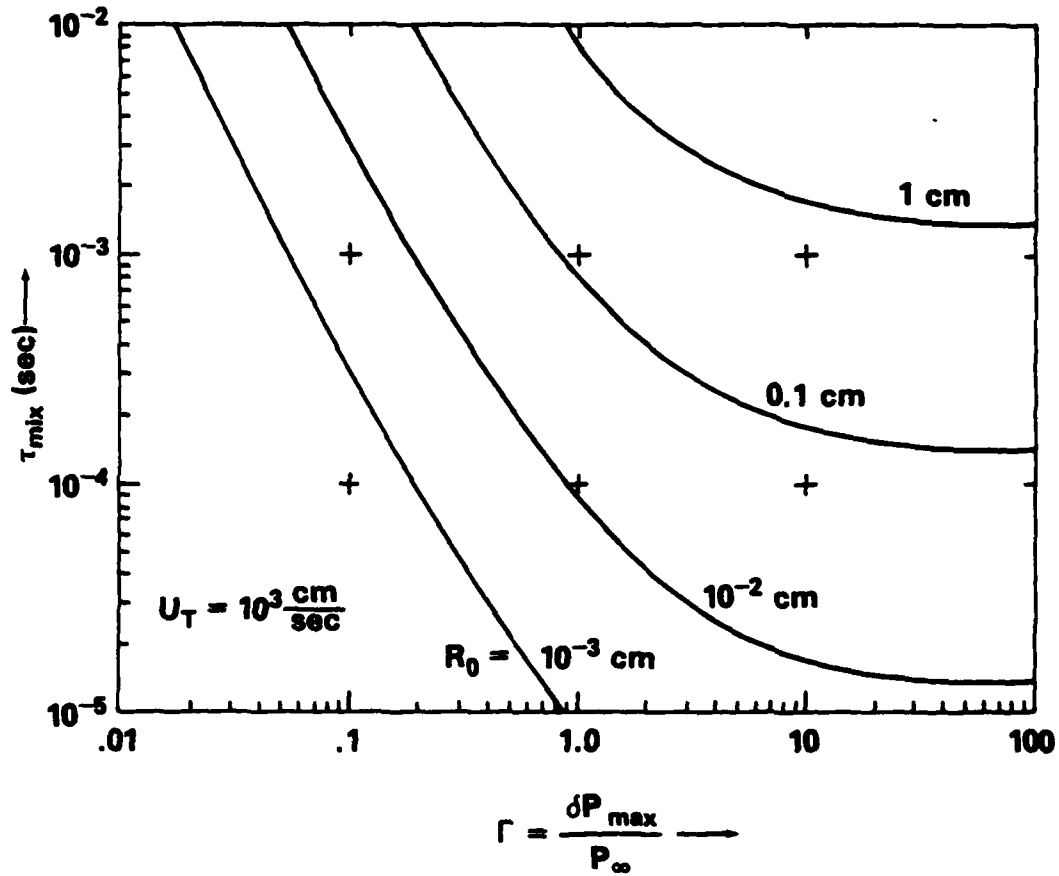


Fig. 17 — Mixing time estimates as a function of pulse overpressure  $\Gamma$  and initial beam radius  $R_0$ .  $U_T = 10^3$  cm/sec is generally characteristic of air at STP. The formulae summarized in Section V were used with  $|f_2| = \frac{1}{5}$  and  $C_s \approx 5 \times 10^4$  cm/sec.

DISTRIBUTION LIST

1. Commander  
Naval Sea Systems Command  
Department of the Navy  
Washington, D.C. 20363  
Attn: NAVSEA 03H (Dr. C. F. Sharn)
2. Central Intelligence Agency  
P. O. Box 1925  
Washington, D.C. 20013  
Attn: Dr. C. Miller/OSI
3. Air Force Weapons Laboratory  
Kirtland Air Force Base  
Albuquerque, New Mexico 87117  
Attn: Lt. Col. J. H. Havey
4. U. S. Army Ballistics Research Laboratory  
Aberdeen Proving Ground, Maryland 21005  
Attn: Dr. D. Eccleshall (DRXBR-BM)
5. Ballistic Missile Defense Advanced Technology Center  
P. O. Box 1500  
Huntsville, Alabama 35807  
Attn: Dr. L. Havard (BMDSATC-1)
6. B-K Dynamics, Inc.  
15825 Shady Grove Road  
Rockville, Maryland 20850  
Attn: Mr. I. Kuhn
7. Intelcom Rad Tech  
P. O. Box 81087  
San Diego, California 92138  
Attn: Mr. W. Selph
8. Lawrence Livermore Laboratory  
University of California  
Livermore, California 94550  
Attn: Dr. R. J. Briggs  
Dr. T. Fessenden  
Dr. E. P. Lee
9. Mission Research Corporation  
735 State Street  
Santa Barbara, California 93102  
Attn: Dr. C. Longmire  
Dr. N. Carron

10. National Bureau of Standards  
Gaithersburg, Maryland 20760  
Attn: Dr. Mark Wilson
11. Science Applications, Inc.  
1200 Prospect Street  
La Jolla, California 92037  
Attn: Dr. M. P. Fricke  
Dr. W. A. Woolson
12. Science Applications, Inc.  
Security Office  
5 Palo Alto Square, Suite 200  
Palo Alto, California 94304  
Attn: Dr. R. R. Johnston  
Dr. Leon Feinstein
13. Science Applications, Inc.  
1651 Old Meadow Road  
McLean, Virginia 22101  
Attn: Mr. W. Chadsey
14. Science Applications, Inc.  
8201 Capwell Drive  
Oakland, California 94621  
Attn: Dr. J. E. Reaugh
15. Naval Surface Weapons Center  
White Oak Laboratory  
Silver Spring, Maryland 20910  
Attn: Mr. R. J. Biegalski  
Dr. R. Cawley  
Dr. J. W. Forbes  
Dr. D. L. Love  
Dr. C. M. Huddleston  
Dr. G. E. Hudson  
Mr. W. M. Hinckley  
Mr. G. J. Peters  
Mr. N. E. Scofield  
Dr. E. C. Whitman  
Dr. M. H. Cha  
Dr. H. S. Uhm  
Dr. R. Fiorito
16. C. S. Draper Laboratories  
Cambridge, Massachusetts 02139  
Attn: Dr. E. Olsson  
Dr. L. Matson
17. M.I.T. Lincoln Laboratories  
P. O. Box 73  
Lexington, Massachusetts 02173  
Attn: Dr. J. Salah

18. Physical Dynamics, Inc.  
P. O. Box 1883  
La Jolla, California 92038  
Attn: Dr. K. Brueckner
19. Office of Naval Research  
Department of the Navy  
Arlington, Virginia 22217  
Attn: Dr. W. J. Condell (Code 421)
20. Avco Everett Research Laboratory  
2385 Revere Beach Pkwy.  
Everett, Massachusetts 02149  
Attn: Dr. R. Patrick  
Dr. Dennis Reilly
21. Defense Technical Information Center  
Cameron Station  
5010 Duke Street  
Alexandria, VA 22314 (12 copies)
22. Naval Research Laboratory  
Washington, D.C. 20375
  - M. Lampe - Code 4792 (50 copies)
  - M. Friedman - Code 4700.1
  - J. R. Greig - Code 4763
  - I. M. Vitkovitsky - Code 4770
  - J. B. Aviles - Code 4665
  - M. Haftel - Code 4665
  - T. Coffey - Code 4000
  - Superintendent, Plasma Physics Div. - Code 4700 (25 copies)
  - Branch Head, Plasma Theory Branch - Code 4790
  - Library - Code 2628
  - A. Ali - Code 4700.1
  - D. Book - Code 4040
  - J. Boris - Code 4040
  - I. Haber - Code 4790
  - S. Kainer - Code 4790
  - A. Robson - Code 4760
  - P. Sprangle - Code 4790
  - D. Colombant - Code 4790
  - M. Picone - Code 4040
  - D. Spicer - Code 4169
  - M. Raleigh - Code 4760
  - R. Pechacek - Code 4763

23. Defense Advanced Research Projects Agency  
1400 Wilson Blvd.  
Arlington, VA 22209  
Attn: Dr. J. Mangano  
Dr. J. Bayless
24. JAYCOR  
205 S. Whiting St.  
Alexandria, VA 22304  
Attn: Drs. D. Tidman  
R. Hubbard  
J. Guillory
25. JAYCOR  
Naval Research Laboratory  
Washington, D.C. 20375  
Attn: Dr. R. Fernsler - Code 4770  
Dr. G. Joyce - Code 4790  
Dr. S. Goldstein - 4770
26. SAI  
Naval Research Laboratory  
Washington, D.C. 20375  
Attn: A. Drobot - Code 4790  
W. Sharp - Code 4790
27. Physics International, Inc.  
2700 Merced Street  
San Leandro, CA.  
Attn: Drs. S. Putnam  
E. Goldman
28. Mission Research Corp.  
1400 San Mateo, S.E.  
Albuquerque, NM 87108  
Attn: Dr. Brendan Godfrey
29. Princeton University  
Plasma Physics Laboratory  
Princeton, NJ 08540  
Attn: Dr. Francis Perkins, Jr.
30. McDonnell Douglas Research Laboratories  
Dept. 223, Bldg. 33, Level 45  
Box 516  
St. Louis, MO 63166  
Attn: Dr. Michael Greenspan

31. Cornell University  
Ithaca, NY 14853  
Attn: Prof. David Hammer
32. Sandia Laboratories  
Albuquerque, NM 87185  
Attn: Dr. Bruce Miller  
Dr. Barbara Epstein
33. University of California  
Physics Department  
Irvine, CA 92717  
Attn: Dr. Gregory Benford
34. Defense Technical Information Center  
Cameron Station  
5010 Duke Street  
Alexandria, VA 22314 (12 copies)
35. Beers Associates Inc.  
Attn: Dr. Douglas Strickland  
P. O. Box 2549  
Reston, Va, 22090